

**PHOTOACOUSTIC IMAGING AND HIGH INTENSITY FOCUSED
ULTRASOUND IN BIOMEDICAL APPLICATIONS**

By

JANGGUN JO

Submitted to the graduate degree program in Bioengineering Program and the Graduate
Faculty of the University of Kansas in partial fulfillment of the requirements for the
degree of Doctor of Philosophy.

Chairperson Dr. Xinmai Yang

Dr. Carl W. Luchies

Dr. M. Laird Forrest

Dr. Sara Wilson

Dr. Qiang Ye

Date Defended: 05/30/2014

The Dissertation Committee for Janggun Jo

certifies that this is the approved version of the following dissertation:

**PHOTOACOUSTIC IMAGING AND HIGH INTENSITY FOCUSED
ULTRASOUND IN BIOMEDICAL APPLICATIONS**

Chairperson Dr. Xinmai Yang

Date Approved: 05/30/2014

Abstract

Optical and acoustical technologies for biomedical devices have been developed rapidly in the past years. These non-invasive technologies are used for diagnostic and therapeutic studies with great potential for improving biomedical applications. In this work, photoacoustic imaging that combines the advantages of optical and ultrasound imaging, and high intensity focused ultrasound (HIFU) treatment enhanced with laser were investigated to understand the application and feasibility of optics and acoustics in biomedical studies. At first, photoacoustic tomography system was used to monitor brain functional activation by monitoring the changes of the blood volume at the cerebral cortex surface of rats induced by cocaine hydrochloride. And, the research was continued with a photoacoustic microscopy (PAM) system. With the PAM system, the brain images were obtained at coronal views, and the regional changes in the total hemoglobin (HbT) concentration were presented. Additionally, a customized photoacoustic imaging system was applied to detect the neuronal activity in the motor cortex of an awake, behaving monkey during forelimb movement. The research results that showed the activated region images demonstrated the capability of photoacoustic imaging. Next, photoacoustic wave propagation was studied using shock wave theory. The propagation was analyzed in non-linear way and simulated to compare the difference between existing linear and non-linear solutions. Further, the combination of laser and HIFU treatment was studied. Cavitation activities and increase of temperature during HIFU treatment were investigated by using *in vivo* murine animal models. The enhanced results from the HIFU treatment with laser illumination showed the efficacy and potential of the system. The

studies of PA imaging and HIFU treatment demonstrate the high feasibility of using optics and acoustics in the biomedical area.

Acknowledgements

This dissertation would not have been possible without the help and guidance of many people. I wish to leave a message of my thanks to them on the acknowledgements of the dissertation. I will be always grateful to my Committee Chair, Dr. Xinmai Yang. He has guided, support, and taught me during my entire Ph.D. program. This dissertation was completed with his help. And, my committee also provided invaluable support and insight over the last four years. I would like to thank my committee members, Dr. Carl Luchies, Dr. Sara Wilson, Dr. Qiang Ye, and Dr. Laird Forrest. They have also helped me with their comments and suggestions since I met them. I really appreciate them.

Additionally, I am thankful to my wife, Suk Jung, and my parents for their support and love. My abroad study in KU has started with trust and support of my parents. And, I have enjoyed the wonderful life in Lawrence Kansas with my wife. She always supports me to study and do my best in KU. And, I appreciate Dr. Hyunchan Cho, and Dr. Kwangsun Kim, who recommended me to study in KU. After I came to KU, I received lots of concerns and helps from friends, and other faculties. I appreciate all of them and say goodbye. I will miss them after I move to Michigan.

Table of Contents

Abstract.....	ii
Acknowledgements	iv
Table of Contents	v
List of Table Captions	ix
List of Figure Captions.....	x
Chapter 1 Introduction	1
1.1 Background and motivation.....	1
1.2 The goal of this research	4
Chapter 2 Detection of cocaine induced rat brain activation by photoacoustic tomography	6
2.1 Introduction.....	6
2.2 Materials and Methods.....	8
2.2.1 Photoacoustic tomography system.....	8
2.2.2 Animal preparation	10
2.2.3 Imaging process	11

2.3 Results.....	11
2.4 Discussion and Conclusions	16

**Chapter 3 Functional photoacoustic imaging to observe regional
brain activation induced by cocaine hydrochloride..... 18**

3.1 Introduction.....	18
3.2 Materials and methods	19
3.3 Results and Discussion	24
3.4 Conclusions.....	29

**Chapter 4 Photoacoustic detection of functional responses in the
motor cortex of awake behaving monkey during forelimb
movement 31**

4.1 Introduction.....	31
4.2 Materials and methods	32
4.3 Results.....	37
4.4 Discussion and Conclusions	41

Chapter 5 The propagation of photoacoustic shock wave 43

5.1 Introduction.....	43
5.2 Methods.....	45

5.2.1 Linear solution	45
5.2.1 Nonlinear solution.....	47
5.3 Results and Discussion	50
5.3.1 Nonlinear propagation of PA waves	50
5.3.2 Comparison between linear and shock wave solutions.....	52
5.4 Conclusions.....	55

**Chapter 6 Laser-enhanced high-intensity focused ultrasound heating
in an *in vivo* small animal model..... 57**

6.1 Introduction.....	57
6.2 Methods.....	59
6.2.1 Experiment setup	59
6.2.2 Animal model.....	61
6.2.3 Experiment procedure.....	62
6.3 Results.....	63
6.3.1 Temperature enhancement.....	63
6.3.2 Cavitation enhancement.....	70
6.4 Discussion.....	73
6.5 Conclusions.....	76

Chapter 7 Conclusions..... 78

7.1 Summary and Conclusions78

7.1.1 The results of PA imaging78

7.1.2 The results of laser-enhanced HIFU79

7.2 Future Work.....79

7.2.1 Contrast agent for absorption.....80

7.2.2 Application for humans.....80

7.2.3 Other techniques using optics and acoustics.....81

Bibliography 82

Vita

List of Table Captions

Table 6.1 Number of HIFU lesions with clear cavitation acoustic emissions from five HIFU sonications.	72
---------------------------------------------------------------------------------------------------------------	----

List of Figure Captions

- Figure 2.1 Schematic of the PAT system used for imaging in a rat brain in vivo. 10
- Figure 2.2 Non-invasive PAT imaging of a rat's cerebral cortex: (a) before the injection of cocaine hydrochloride; (b) 60 min after the injection of 5mg/kg concentration cocaine hydrochloride; (c) a pixel-wise differential image (image b and image a); (d) an open-skull photograph of the rat's cerebral cortex.13
- Figure 2.3 Averaged photoacoustic signal amplitude increases at cerebral cortex of rats. Three concentrations of cocaine hydrochloride are used: 0 (pure saline solution), 2.5, and 5.0 mg/kg body weight. The error bars are standard deviations from the average of the five animals in each group.15
- Figure 3.1 Schematic of the PAM system used for imaging in a rat brain in vivo.20
- Figure 3.2 PA B-scan image of a rat's brain at 3.2 mm posterior to bregma.23
- Figure 3.3 Averaged photoacoustic signal amplitude increases (PAM). Two concentrations of cocaine hydrochloride are used: 3, and 5.0 mg/kg body weight. (N=4).....23
- Figure 3.4 Functional images (ΔI_F) at 1.2 mm posterior to bregma, and 3.4 mm posterior to bregma. sO_2 changes are observed at 10, 20, and 30 min. The negative values in ΔI_F indicated the increases in sO_2 levels, and vice versa.26
- Figure 3.5 Photographs taken prior to (a), right after (b), 5 days after (c) and 16 days (d) after HIFU treatment. All photos are at the same length scale. ..28

Figure 4.1 The imaging position. central sulcus (CS), arcuate sulcus (AS) and the precentral dimple (PcD). (a) Motorized scanner (b) The position of the cortical chamber on the monkey brain (c) 3D MRI image and enlarged view of the revealed within the chamber (d) a photo of a representative example of geometry from the paper published in 1997 by Gail Widener and Paul Cheney.34

Figure 4.2 Time sequence of data acquisition and HIFU waves.36

Figure 4.3 PA images of functional activity in primary motor cortex and primary somatosensory cortex of a macaque monkey. Color scale indicates the amplitude of the detected PA signal with “1” indicating the maximal value. (a) Reference image acquired with the behavioral task off. Primary motor cortex (M1), primary somatosensory cortex (SI) and the location of the central sulcus (CS) are identified. (b) Image obtained over the same region of the cortex while the monkey was performing a reach-to-grasp task with its contralateral forelimb. (c) Overlay of the PA image obtained during movement on an MRI image of the monkey’s brain. The dark line circle shows the position of the rim of the cranial chamber. (d) Changes in the average PA signal obtained from M1 and SI cortex averaged over the regions outlined by the dotted lines in (a) and (b). Note that the area encompassed by the dotted line is largely M1 but includes a small part of premotor cortex anteriorly. (e) PA B-mode functional image superimposed on an MRI cross-section through the central sulcus. The black line in Figure 4.3(a) shows the location and orientation of the section. The B-mode image was acquired with the task off. The dimension of the PA image is 12 x 12 mm. (f) The same image as (e) but obtained during performance of the reach-to-grasp task. .40

Figure 5.1 Changes of the linear propagating spherical waveforms generated from sphere target on the different distances.....	46
Figure 5.2 Distortion of propagating plane shock waveforms. Dashed line displays theoretical waveform. Solid line is the waveform with equal-area rule applied (the actual waveform). The amplitude of pressure is normalized by the initial pressure (p/p_0).....	48
Figure 5.3 Change of N-waveform applied the shock wave solution for plane wave (a~c) and spherical wave (d~f). The dotted line and the solid line indicate the distorted photoacoustic wave and the shock wave with equal-area rule (the actual waveform).	51
Figure 5.4 The propagating PA spherical waves on the different distance. The dashed line indicates the linear spherical wave, and the solid line indicates spherical shock wave.	52
Figure 5.5 Photoacoustic signal from a black hair detected by a standard needle hydrophone. The peak amplitude is equal to 1.17 MPa at 10 MHz, which is the center frequency of the signal.	53
Figure 5.6 Comparison of the peak amplitude of the pressure between linear and nonlinear spherical wave models. (a) Pressure amplitude, and (b) ratio between nonlinear and linear solution	54
Figure 5.7 The relative error between the amplitude of the linear and non-linear spherical wave solution with (a) different radii of target sphere, and (b) different initial pressures.....	55
Figure 6.1 Schematic of the PAI-guided HIFU system.	60
Figure 6.2 Measured Temperatures and error with standard deviation. (a) The time profile of temperature change. (b) The temperature difference between average results from HIFU with and without laser exposure.	64

Figure 6.3 Photograph of HIFU lesions. HIFU treatments with laser and without laser were implemented in 5 mm depth from the skin. The leg muscle was cut open to show the enhanced necrosis by HIFU with laser.	65
Figure 6.4 Temperature enhancement rates in different wavelengths, depths and HIFU pressure.	68
Figure 6.5 Comparison of the temperature enhancement rates for different HIFU durations. (a) The enhancement rates of laser-enhanced HIFU in 2 mm and 9 mm depths for 2 seconds and 10 seconds. (b) The enhancement rates in 532 nm and 760 nm of wavelength of laser for 2 seconds and 10 seconds.	69
Figure 6.6 Cavitation signals detected by a PCD as a function of time. (a) The signal generated with HIFU -only. (b) The signal generated with HIFU and laser exposure using the same pressure. 20mJ/cm ² fluence and 532 nm wavelength laser and 7.9 MPa HIFU pressure were used at 2 mm depth.	71
Figure 6.7 Photoacoustic pressure generated from rat blood in a tubing.	74

Chapter 1 Introduction

1.1 Background and motivation

Recently, expertise in advanced optical and acoustical technology has been developed and utilized for a wide range of biomedical applications. Diagnostic studies apply optic and acoustic property to imaging and detection of diseases, conditions and illnesses such as diagnosis of cancerous lesions, guidance of diagnostic biopsies, and targeting and monitoring of treatment. The use of optical and acoustical techniques in diagnostic studies has potentiated successful applications involving prostate cancer, metastatic disease in lymph nodes, tumors in the eye, breast cancer, blood vessel conditions, and liver disease. Optics and acoustics have also frequently been used for therapeutic studies in applications involving ophthalmic and cardiac diseases, treatment of cancer, brain disorder, etc. These applications are critical for scientists and draw more attention to the biomedical area.

Imaging technologies using optics and acoustics have increased for disease prevention, diagnosis, and treatment. Ultrasound-based diagnostic imaging techniques have been used for over 20 years and have an excellent safety record. Compared to other prominent imaging modalities, ultrasound imaging has several advantages like nonionizing imaging, low-cost and high spatial resolution. An ultrasound image is obtained by sending a pulse of ultrasound and detecting the reflected pulse. Meanwhile, the optical imaging modalities use visible and near-infrared light and the properties of photons (1, 2). Optical property such as scattering and absorption offers the potential to differentiate among soft tissues. And optical images provide a contrast between native

soft tissues and tissues labeled with contrast agents, using optical absorption or scattering spectra at different wavelengths (3). In biological tissue, optical imaging offers great potential for providing specific tissue contrasts as well as capabilities for studying functional and molecular information as the basis for health and disease (4, 5).

Photoacoustic (PA) imaging is a hybrid imaging modality that combines the advantages of optical and ultrasound imaging (6-9). It provides an excellent tissue contrast achieved in optical techniques with the high spatial resolution of ultrasound imaging. PA imaging is based on the photoacoustic effect, which refers to the ultrasound waves generated by the absorption of photons. The PA effect was first reported by Alexander Graham Bell in 1880 (10). Since the mid-1990s, the PA technique has been investigated for biomedical imaging and PA images began to appear thereafter (11-14). Until now, the PA technique has been developed in terms of the design of instrumentation, image reconstruction algorithms, and functional and molecular imaging capabilities and has been applied in various studies of medicine, engineering, and biology. In PA imaging, biological tissue is irradiated with nanosecond pulses of safely modulated laser light, which is absorbed by chromophores in tissue leading to the generation of ultrasound waves. The wave that subsequently propagates can be measured using ultrasound detectors, and can be used to reconstruct PA images. Because ultrasound scattering is two to three times weaker than optical scattering in biological tissues, PA imaging can provide a higher resolution than optical imaging (6, 15).

PA imaging techniques for functional imaging of biological tissues are desirable and the technique has been increasingly employed in studies of neurophysiology,

neuropathology, and neurotherapy. PA imaging can be used in describing tissue structure and disorder, deducing functional parameters in biological tissue, and studying functional cellular and biochemical information via optical absorption and wavelength dependence. PA imaging can provide good images for the structure of small tumors, cancer and blood vessels (12, 16, 17), and PA also detects various intrinsic optical signals caused by changes in blood volume, oxygen consumption, and cellular swelling (18-22). These signals have been associated with brain physiology and pathology. PA imaging provides a non-invasive method to image functional tissue structures and also provides information about regional oxygen consumption and hemodynamics in brains. And multiple studies have demonstrated the capability and potential of functional PA imaging for brain research tracking hemodynamics in the brains of *in vivo* animal models (23-25).

Since the 1940s, therapeutic ultrasound has been used for heating and disruptive effects in tissue (26). The use of ultrasound in the field of medicine started initially with the effects of high intensity ultrasound for therapy rather than diagnosis. High intensity focused ultrasound (HIFU) is one of the non-invasive methods used primarily to treat abnormal tissue thermally through hyperthermia (27-29). During HIFU treatment, the high intensity ultrasound is delivered to the focal region of the HIFU transducer, and subsequently absorbed by the soft tissue there. The absorption of HIFU energy induces a rapid temperature rise, which results in tissue coagulation, and finally leads to irreversible tumor cell death and severe damage to tumor blood vessels in the treated region. (27, 29) The soft tissue outside the focal region will be undamaged because the ultrasound intensity is relatively low in those regions. With imaging systems such as ultrasound imaging and magnetic resonance imaging (MRI), the use of HIFU has been extended.

Since the treatment of bladder cancers with HIFU has been attempted, HIFU has been used as an effective treatment for ablation of several types of cancers (27, 28, 30-36).

The clinical applications using optics and acoustics have rapidly grown in biomedical fields with the advantages of safety and non-invasive diagnostics and therapeutic procedures. The utilization of ultrasound-based applications has already been widespread in medicine. And the optical imaging market is expected to grow by as much as \$1.9 billion in five years. Along with other researchers, I am interested in the studies of optical and acoustical techniques in the biomedical area. The PA imaging modality and HIFU system is discussed and investigated in this dissertation.

1.2 The goal of this research

In this study, we first demonstrate that the functional PA imaging system can be used to detect brain activity. Photoacoustic tomography (PAT) and photoacoustic microscopy (PAM) are used to detect progressive changes in the cerebral cortex of a rodent's brain after the administration of cocaine hydrochloride. The functional PA images are compared and confirm the hemodynamic changes in the brain. In addition, PA imaging is applied to detect the neuronal activity in the motor cortex of an awake, behaving monkey during forelimb movement. An increase in regional blood volume is interpreted as increased neuronal activity. These results of functional PA images demonstrate the feasibility of utilizing PA imaging for brain research.

Secondly, the quantitative study for non-linear propagation of PA waves will be discussed. To accurately estimate the amplitude of the initial PA waves when they are generated, the propagation of PA waves has been modeled by using linear acoustic theories although the generated PA waves are naturally shock waves, whose dissipation mechanism is different from linear waves. Therefore, shock wave dissipation will be considered to accurately recover the amplitude of the initial PA waves. The propagation of photoacoustic shock waves are investigated by using nonlinear acoustic wave solutions and are simulated to show the difference between the linear and nonlinear solutions.

Finally, the HIFU system will be improved with the concurrent use of laser illumination. We further investigate the enhanced heating effect when a diagnostic laser system is used concurrently with HIFU in *in vivo* murine animal experiments. The cavitation activities and enhanced temperature will be detected to show the efficacy and potential of laser-enhanced HIFU in this study.

Chapter 2 Detection of cocaine induced rat brain activation by photoacoustic tomography

2.1 Introduction

Chronic drug abuse and addiction cause serious harm to the society and the addicted individuals (37, 38). The adaptations that occur in brain structure and function caused by chronic drug use appear to be long-lasting and implicate multiple brain circuits (39). New behavioral and pharmacological treatments need to be developed to treat such neuroadaptations. However, the development of new pharmacological interventions requires understanding the effects of potential medications in a neural system. Because small animals have been widely used as laboratory models to study neuroadaptations and pharmacological interventions, there are clear needs for sensitive methods to globally map the effects of pharmacological actions on central nervous system in small animals. The imaging methods used to detect the brain functional changes in small animal models for drug abuse/addiction include fMRI and PET, these techniques associate with either high cost or using ionizing radiations.

High-resolution optical imaging also has been widely applied in small animal studies of basic brain function and diseases. However, due to strong light scattering in soft tissue, high-resolution, purely-optical imaging modalities usually only have an imaging depth of ~1 mm in soft tissue. As a result, the application of high-resolution, purely-optical imaging for small animal brain studies often requires removing or thinning the skull, which are invasive procedures associated with significant risks and draw-backs.

Photoacoustic tomography (PAT) (also referred as thermoacoustic (40), or optoacoustic tomography (16)) overcomes the limitations of other existing optical imaging modalities and combines optical contrast with ultrasonic resolution. PAT is based on the generation of photoacoustic waves by safely depositing short-pulsed optical energy into tissue. Each laser pulse causes a rapid temperature rise on the order of 10 millidegrees. The ultrasonic emission due to thermoelastic expansion can be detected with a single-element ultrasonic transducer or an array of ultrasonic transducers and then used to reconstruct an image (41). In PAT, the task is to determine the relative optical absorption density (or specific absorption) distribution from the measured photoacoustic data, i.e., to map the optical absorption heterogeneity of the tissue. PAT can provide images with optical contrast and ultrasound resolution in regions up to 5 cm deep (42).

PAT has been used in *in vivo* small animal experiments for noninvasive monitoring of angiogenesis, blood oxygenation, and functional changes in the brain (7, 43). In this paper, for the first time to the authors' knowledge, PAT is applied to detect the activation of the brain function induced by using of cocaine in small animals. Brain activation due to cocaine abuse in small animals has been one of popular models to study drug abuse/addiction, and cocaine is one of most commonly use addictive drugs. With repeated use, cocaine can lead to addiction. Cocaine administration produced a dose-dependent neuronal activation that is accompanied by changes in brain metabolic rate. More specifically, acute cocaine administration will affect the level of dopamine in the brain, and as a result, changes in cerebral blood volume will be induced. Many studies in the past have demonstrated regionally restricted activation in the brain of small animals after acute cocaine administration with fMRI. PAT, with all the merits aforementioned,

has the potential to be an alternative imaging modality for this application, and provide complementing information to fMRI and PET.

In this study, we use PAT to monitor brain functional activation by monitoring the changes of the blood volume at the cerebral cortex surface of small animals. In blood, PA signal is mainly determined by the concentration of hemoglobin. During the performance of PAT, we used 797 nm optical wavelength light, which is an isospectral point, i.e., the wavelength that the optical absorption levels of oxygenated hemoglobin (HbO₂) and deoxygenated hemoglobin (Hb) are the same, and therefore, the obtained photoacoustic signal amplitude are proportional to the local blood volume (43, 44). As a result, the changes in blood volume can be detected by monitoring the amplitude changes of the detected photoacoustic signals. On a PAT image, the changes in photoacoustic signal amplitude will result in the changes in image contrast.

2.2 Materials and Methods

2.2.1 Photoacoustic tomography system

We used a photoacoustic tomography (PAT) system, and the schematic of the system is shown in Figure 2.1. The PAT system has a tunable OPO laser (Surelite OPO PLUS; Continuum, Santa Clara, CA) pumped by an Nd:YAG laser (Surelite III; Continuum, Santa Clara, CA) that provided 10 Hz laser pulses with 6 ns pulse width. The laser beam was expanded and homogenized by a diffuser lens (grounded glass). The incident energy density of the laser that reached the surface of the rat head was less than

20 mJ/cm², which complied the safety limit for human skin exposure (45). We used 797 nm wavelength of laser to illuminate shaved rat head, which emits ultrasound due to photoacoustic effect. The generated photoacoustic signals from the rat's brain were detected by 5-MHz unfocused ultrasonic transducers (V310, Olympus NDT, Waltham, MA) which were scanned around the rat's head horizontally (44, 46). Two transducers were used during data acquisition. The two transducers were set apart by 180°, and carefully aligned to face the scanning center. As a result, each transducer only needed to scan 180° to get a full circular scan. The detected signals were amplified by a multi-channel pre-amplifier, collected through a multiple-channel data acquisition board (Gage, Lockport, IL), and then downloaded to a personal computer for post-analysis. During data collection, a stepper motor was controlled to rotate two ultrasonic transducers. The scanning step was 2 degrees with 20-time average. Data collected through the two ultrasonic transducers was combined and compensated by laser power level that is measured by photo diode for imaging reconstruction. The system was able to acquire one PAT image every five minutes. In order to monitor the changes in the rat brain continuously, PAT system had to continuously run to obtain the data periodically.

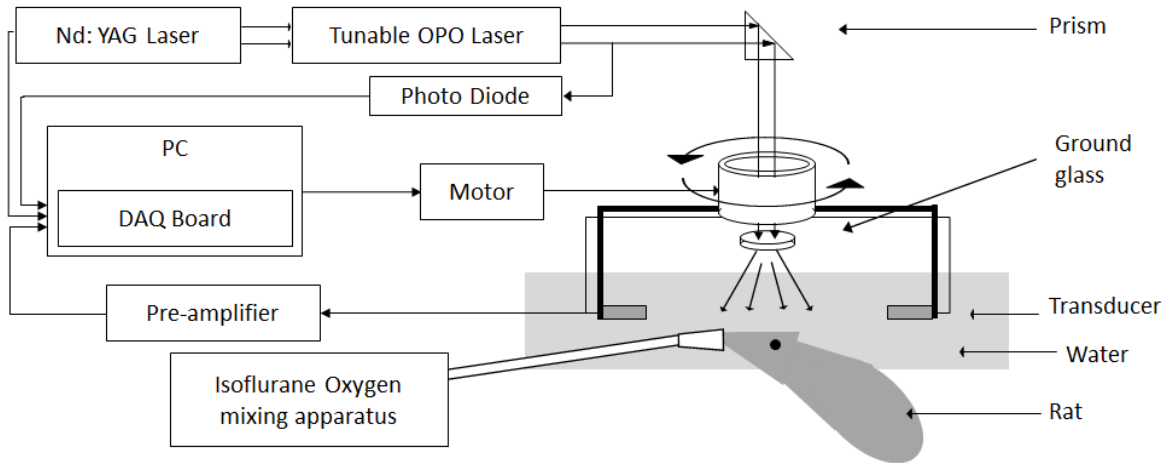


Figure 2.1 Schematic of the PAT system used for imaging in a rat brain in vivo.

2.2.2 Animal preparation

Sprague Dawley rats were used as our animal model. For imaging procedures, animals were initially anesthetized with a mixture of ketamine (87mg/kg body weight) and xylazine (13mg/kg body weight), the subsequent anesthesia (about one hour after the initial anesthesia) was maintained with the inhalation of 1.0~2.0 % isoflurane mixing with oxygen. The hairs on the head of animal were shaved with an electric shaver first, and then the hair removal lotion were applied to depilate the rest of hairs. At the end, the lotion was wiped away with gauzes and followed by washing with warm water. The procedure was repeated until the hairs were completely removed. At this point, the animals were kept under anesthesia with a gas anesthesia machine during the balance of the experiment. Surgical tapes were used to gently secure the animal onto a warmed pad

and secured in the imaging aperture in which only light pressure was needed. A custom-designed surgical stereotaxic frame was also used to fix the head of the animal with ear-pins and a tooth-pin. The body temperature was maintained with a heating lamp. The heartbeat of the animal remained about 250 ± 10 per minute.

2.2.3 Imaging process

For the *in vivo* animal experiment, fifteen Sprague-Dawley rats (140 g to 220 g body weight) were used, and the details for animal preparation are also presented in supplementary information. These rats were divided into 3 groups and injected cocaine hydrochloride in 0.9% sterile saline at given dose of 0 (sham treatment, saline only), 2.5, and 5.0 mg/kg body weight respectively. Totally, each animal was given 0.9% sterile saline at a dose of 1 ml/kg body weight. About two hours after administering the initial anesthesia, the cocaine hydrochloride in sterile saline solution was injected through the rat tail veins. During the experiment, the heart rate and blood oxygenation was monitored with a pulse-oximeter (Nonin medical, PulseSense VET, Plymouth, MN). An initial PAT image was obtained right before the injection of cocaine hydrochloride solution. This image would serve as the reference image. Then the drug was injected and PAT was performed continuously for a total period of at least 60 minutes.

2.3 Results

As the first step, we tested PA signals generated from cocaine hydrochloride solution at 797 nm. The concentration of cocaine in saline solution is 1.65×10^{-5} mol/ml that

has the similar concentration with the case of 5 mg/kg (body weight) of cocaine. The signal from the solution was indistinguishable from noise, and therefore, the optical absorption of cocaine hydrochloride solution is negligible.

The example of obtained PAT image of brain cortex surface is shown in Figure 2.2. Figure 2.2(a) and 2.2(b) were taken before and 60 minutes after the injection of 5 mg/kg cocaine hydrochloride, respectively. Compared with Figure 2.2(a), Figure 2.2(b) reveals the brain vasculature with greater clarity. This enhanced clarity is the result of the brain function activation due to the injection of cocaine hydrochloride, which stimulates the central nervous system and causes the increase of blood flowing into the brain. Consequently, the amplitudes of the detected photoacoustic signals will increase, and hence the contrast between blood in vessels and the background brain tissues will be enhanced. A differential image shown in Figure 2.2(c) was obtained by subtracting the amplitude of the pre-injection data (Figure 2.2(a)) from that of the post-injection data (Figure 2.2(b)) and reconstructing. This image displays the distribution of differential optical absorption (i.e., the changes in blood volume) in the rat brain as induced by cocaine hydrochloride. All the PAT images of the rat brain match well with the open-skull anatomical photograph in Figure 2.2(d).

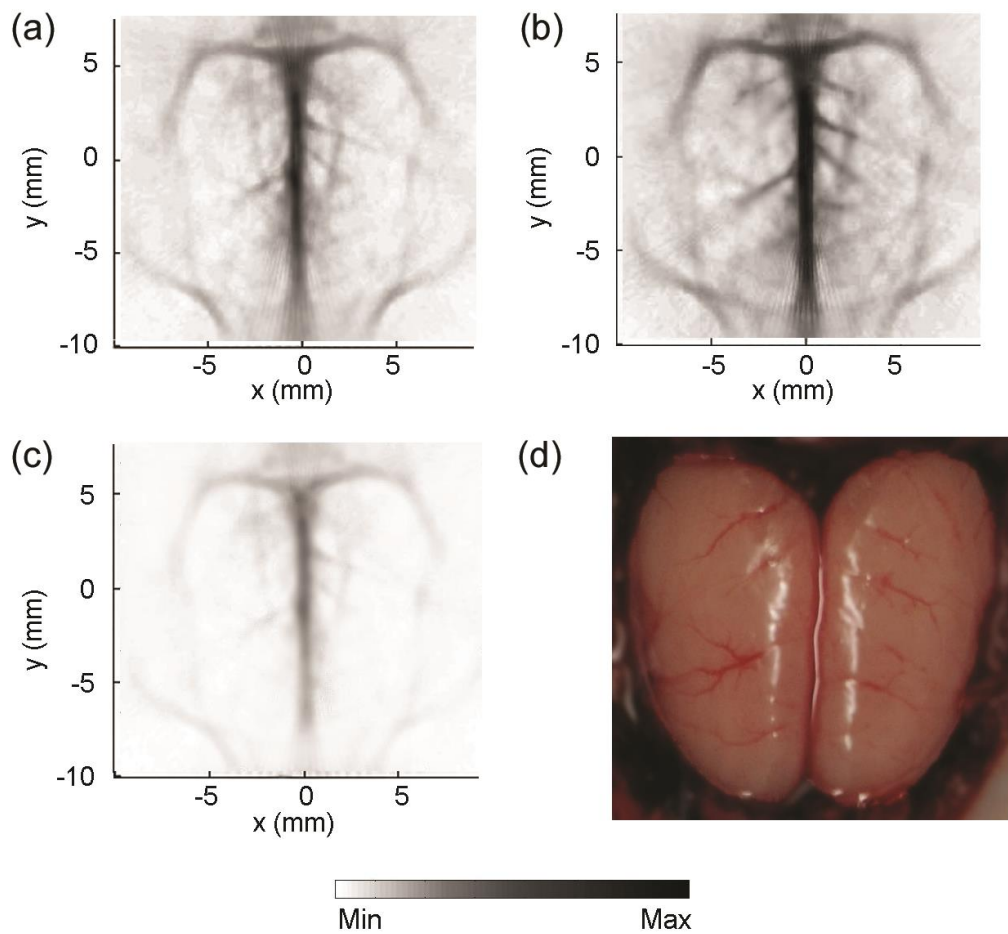


Figure 2.2 Non-invasive PAT imaging of a rat's cerebral cortex: (a) before the injection of cocaine hydrochloride; (b) 60 min after the injection of 5mg/kg concentration cocaine hydrochloride; (c) a pixel-wise differential image (image b and image a); (d) an open-skull photograph of the rat's cerebral cortex.

The changes in the amplitudes of photoacoustic signals after cocaine hydrochloride injection were calculated for all PAT images. The signals were integrated over each image and then normalized to the signal integration of the reference image. The signal increases are presented in percentage, with 0% indicates no increase comparing with the reference signal. Figure 2.3 shows the results of the changes in photoacoustic signal amplitudes averaged on brain cortex after the injection of three concentrations (0 mg/kg, 2.5 mg/kg, and 5 mg/kg) of cocaine hydrochloride. We notice that after the injection of sterile saline solution (1 ml/kg body weight) without cocaine hydrochloride, the amplitudes of photoacoustic signals decline, and stay at a constant level for up to 60 minute before it starts to come back to the original level. This could be due to physiological reaction as the decreases of the hemoglobin concentration under isoflurane anesthesia. This result will serve as the base line reference for the estimation of the brain response solely due to the injection of cocaine hydrochloride.

The results from the injection of 2.5 mg/kg cocaine hydrochloride shows the decrease on the amplitude of PA signals right after the injection, and the amplitude of PA signals recovers after about 10 minutes. Since PA signal amplitude is related to the blood volume, therefore, this result indicates a decrease in blood volume on brain cortex right after the injection of cocaine hydrochloride, and a recovery in blood volume 10 minutes later. The initial decrease in blood volume on the brain cortex is consistent with the reported result that acute cocaine injection may decrease the cerebral blood volume (47). For 5 mg/kg cocaine hydrochloride injection, however, and we did not observe the initial

decrease in the PA signal amplitude, instead, the PA signal amplitude increases after the injection. This result may be due to the high concentration of cocaine hydrochloride we used. The error bars showed in Figure 2.3 are the standard deviations of the measurements from five animals.

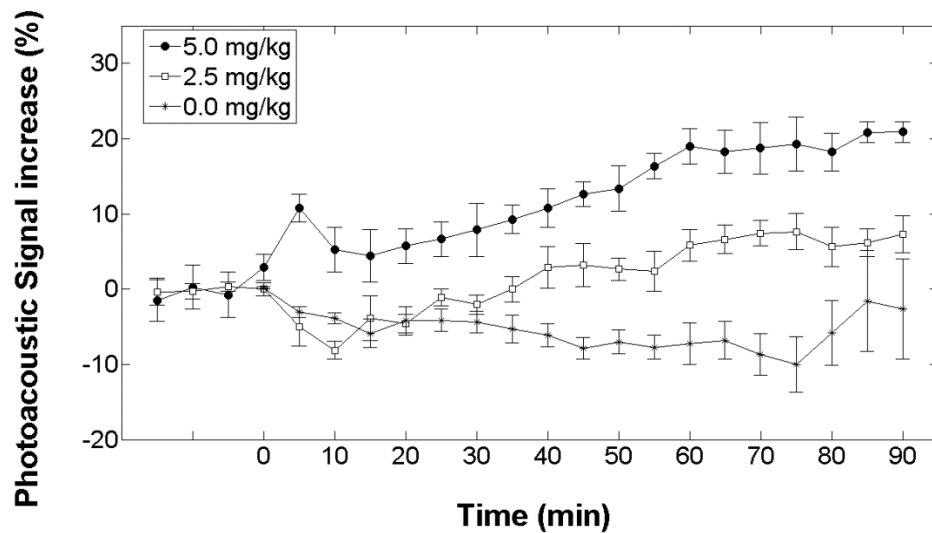


Figure 2.3 Averaged photoacoustic signal amplitude increases at cerebral cortex of rats. Three concentrations of cocaine hydrochloride are used: 0 (pure saline solution), 2.5, and 5.0 mg/kg body weight. The error bars are standard deviations from the average of the five animals in each group.

2.4 Discussion and Conclusions

This research showed PAT is feasible for the study of brain activation due to drug abuse. The major advantage of the PAT brain imaging is the combination of optical contrast and ultrasound resolution in deep regions. The ability of providing non-invasive brain functional imaging by PAT offers an important tool for small animal research. PAT has also demonstrated the ability of imaging through a much thicker monkey brain (48). Therefore, this technique may also be used to perform human brain imaging, or at least infant brain imaging.

Although current study only used 797 nm wavelength light to measure the changes in blood volume (total hemoglobin), PAT technique can be used to measure HbO₂ and Hb separately when two or more optical wavelengths are used. The separated measurements on HbO₂ and Hb will shed more lights on the brain function activation detection.

Images from our current PAT system produced good cerebral cortex surface images. However, due to the poor resolution on the direction perpendicular to the cortex surface, current system cannot resolve between signals generated from the inside of the brain and signals generated from the cortex surface. A reflection-mode photoacoustic imaging system could be more suitable to image inside of the brain (49).

In summary, PAT was used to detect effects of addicted stimulus due to the injection of cocaine hydrochloride. Stimulation of cocaine induces brain function activation, which results in the crease of total blood volume in the brain. On PAT images, the change of blood volume was detected by monitoring the image contrast enhancement.

Our results show that PAT technique can non-invasively detect the brain function activation induced by drug abuse through detecting the blood volume change in small animals.

Chapter 3 Functional photoacoustic imaging to observe regional brain activation induced by cocaine hydrochloride

3.1 Introduction

The abuse of cocaine can cause insanity, strokes, seizures, and tremors (50-52). Imaging technologies have enabled the investigation of the pharmacological effects of chronic drug usage of cocaine on the brain noninvasively. Small animals have been used as experimental models to understand the effects of acute and chronic drug administration on regional brain function, neuroadaptations, and pharmacological interventions. Medical imaging methods, such as functional magnetic resonance imaging (MRI) and positron emission tomography (PET), have been used to globally map the effects of pharmacological actions on the central nervous system in small animals (53, 54). However, these techniques are associated with either high cost or using ionizing radiations.

Photoacoustic tomography (PAT) has been suggested as an imaging tool to detect the functional changes in the brain of small animal models for drug abuse/addiction (55). The administration of cocaine hydrochloride causes a dose-dependent neuronal activation with changes in brain metabolic rate. The changes in cerebral blood volume, which are affected by the level of dopamine and can be either increased or decreased (56, 57), can be detected by PA detection. Previously, we showed the overall changes in blood volume on the brain cortex surface due to drug abuse with a PAT system. In this paper, a photoacoustic microscopy (PAM) system is applied to detect the regional changes in the brain function induced by the injection of cocaine hydrochloride in small animals. With

the PAM system, the brain images are shown at coronal views, and the regional changes in the total hemoglobin (HbT) concentration are presented. Additionally, the regional changes in blood oxygenation are also imaged.

3.2 Materials and methods

For PAM imaging (58), a tunable OPO laser (Surelite OPO PLUS; Continuum, Clara, California), pumped by a Q-switched Nd:yttrium–aluminum–garnet laser (Surelite III; Continuum, Santa Clara, California) was used to generate laser light. During the conduction of PAM, we used 680 and 797 nm optical wavelength light. At 797 nm wavelength, the absorptions of oxy hemoglobin (HbO₂) and deoxy hemoglobin (Hb) are the same (59), and at 680 nm wavelength, the output power of the OPO laser research maximum. These two wavelengths were chosen for calculating the changes in blood oxygenation. The incident energy density of the laser that reached the surface of the rat head was less than 20 mJ/cm², which complied with the safety limit for human skin exposure (45). During data collection, a laser beam was scanned across the surface, and subsequently generated PA signals were detected by a 5-MHz focused ultrasonic transducer (SU-108-013, Sonic Concepts), which has a focal length of 35 mm and diameter of 33 mm. The detected signals were amplified by a preamplifier (5072PR; Olympus-NDT, Waltham, Massachusetts), and collected through a multiple-channel data acquisition board (CS21G8-256MS; Gage, Lockport, Illinois) that used 8 bit resolution and 500 MS/s of sampling rate, and then downloaded to a personal computer for post-analysis. Photoacoustic images were reconstructed by using the envelope of each scan

line from each scan position of the transducer. Essentially, the envelope of each signal at each scan position was projected in the depth direction. The distance along the depth direction was calculated by multiplying the time of flight by the speed of sound in soft tissue. Figure 3.1 shows the PAM system used in the study.

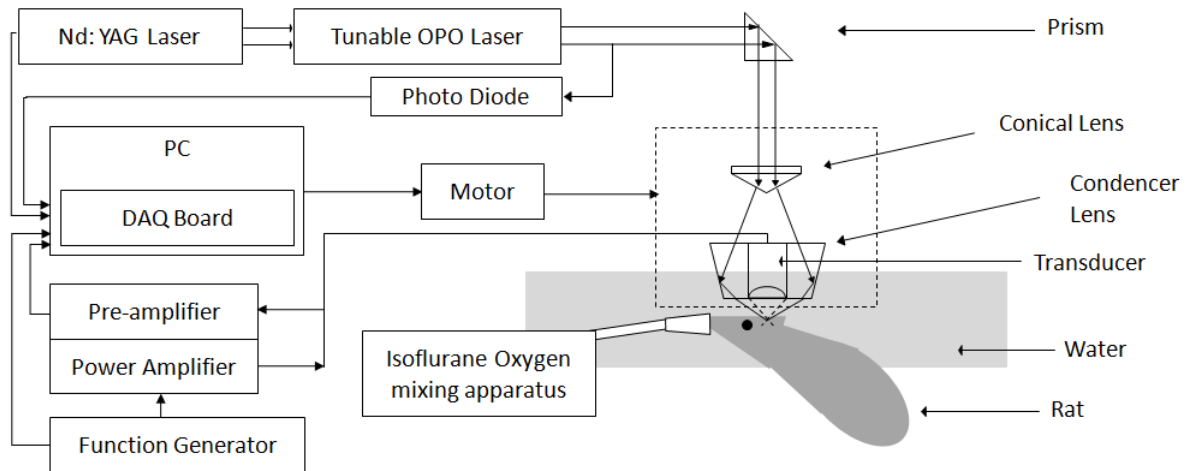


Figure 3.1 Schematic of the PAM system used for imaging in a rat brain in vivo.

Sprague-Dawley rats (140 to 220 g body weight) were used for brain imaging. A total of eight animals were used in the experiments and the images presented here were from one of the animals. For the imaging procedure, the animals were initially anesthetized with a mixture of ketamine (87mg/kg body weight) and xylazine (13mg/kg body weight), and subsequent anesthesia was maintained with the inhalation of 1.0% to 2.0% isoflurane mixed with pure oxygen. After shaving the rat head with an electric

shaver, the anesthetized rat was fixed on a custom-designed surgical stereotaxic frame, and the head surface was coated with ultrasonic gel, and placed under the acoustic coupling membrane in a water tank. The body temperature was maintained using a heating lamp and the heartbeat remained about 250 ± 10 /min. For PAM images, the rat was injected cocaine hydrochloride (Sigma-Aldrich, St. Louis, Missouri) in 0.9% sterile saline at the given dose of 5.0 mg/kg body weight. This dosage of cocaine hydrochloride was chosen because it can produce strong hemodynamic effects. About 2 hours after administering the initial anesthesia, the cocaine hydrochloride in sterile saline solution was injected through the rat tail veins. During the experiment, the heart rate and blood oxygenation were monitored with a pulse-oximeter (Nonin medical, PulseSense VET, Plymouth, Minnesota). An initial PA image before the injection of cocaine hydrochloride solution was obtained to serve as the reference image. Then the drug was injected and PAM was employed to monitor the brain activation continuously. From the initial image, we could identify the coronal suture and confirm the position of bregma with ± 0.2 mm error. All animal handling procedures are approved by the Institutional Animal Care and Use Committee of the University of Kansas.

After the injection of cocaine hydrochloride, the rat brain was scanned with 680 and 797 nm wavelengths. Reference images at 797 nm for a before-injection and an after-injection were acquired and compared with respective images at 680 nm for the same region. The respective images at 680 nm were obtained about 1 min after the reference images at 797 nm. We assumed the changes in brain activation were small during this 1 min because cocaine-induced brain activation is a relatively slow process. To sense the

changes in blood oxygenation (sO₂), functional changes (ΔI_F) were calculated with the following equation (60):

$$\begin{aligned}\Delta I_F &= \frac{I_{(680\text{nm})\text{after injection}}}{I_{(797\text{nm})\text{after injection}}} - \frac{I_{(680\text{nm})\text{before injection}}}{I_{(797\text{nm})\text{before injection}}} \\ &= I_{F\text{after injection}} - I_{F\text{before injection}}\end{aligned}\quad (1)$$

where I denotes the amplitude of PA signals, and I_F denotes the ratio of PA signals at 680 and 797 nm. At 797 nm wavelength, which is an isospectral point for blood, the photoacoustic signal is proportional to the changes in HbT concentration (6). At 680 nm wavelength, the absorption of deoxy-hemoglobin is much higher than that of oxy-hemoglobin. As a result, I_F is inversely proportional to changes in sO₂ and independent of blood volume changes (60). Therefore, the functional change (ΔI_F) reflects the level of sO₂ change. Before calculating ΔI_F , statistical analysis between images obtained at the same wavelength was performed. For the statistical significance, data (p -value of >0.05) were filtered to reduce noise. With the method, PA imaging data from 680 and 797 nm were used to map sO₂ changes by pixel-wise normalization of images (60). ΔI_F is able to signify region of interest for sO₂ changes at two positions, 1.2 mm posterior to bregma and 3.4 mm posterior to bregma.

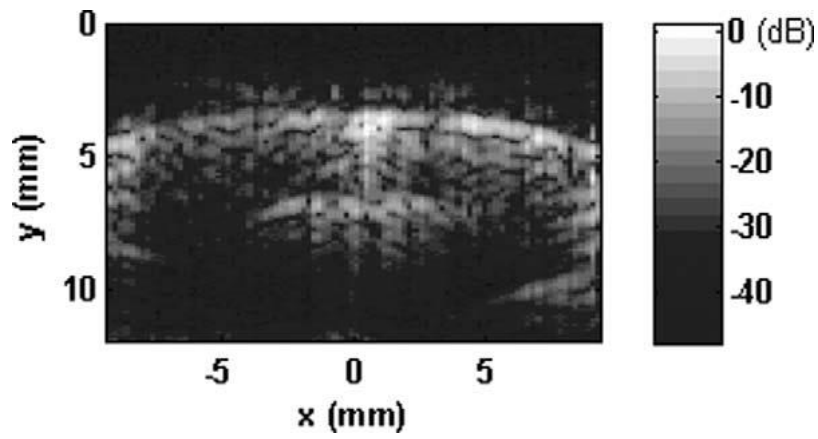


Figure 3.2 PA B-scan image of a rat's brain at 3.2 mm posterior to bregma.

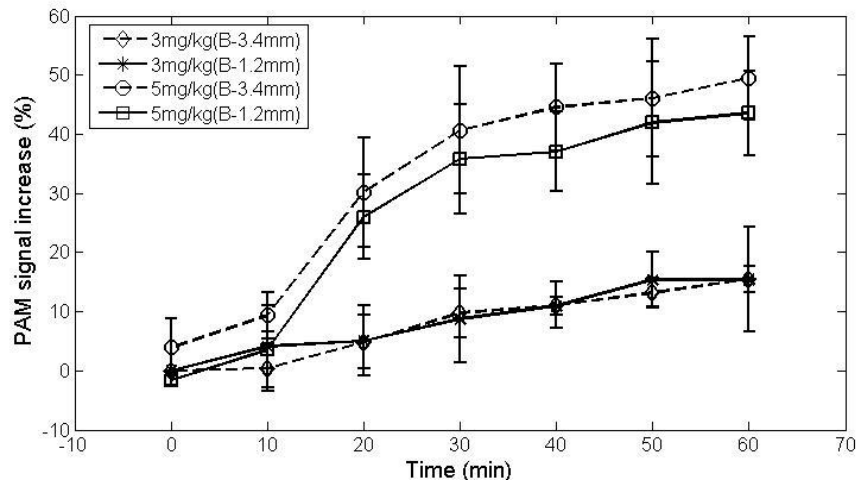


Figure 3.3 Averaged photoacoustic signal amplitude increases (PAM). Two concentrations of cocaine hydrochloride are used: 3, and 5.0 mg/kg body weight. (N=4)

Furthermore, PA imaging data were acquired to investigate the spatiotemporal distribution of relative HbT concentration changes due to the pharmacodynamic effects of cocaine hydrochloride. At 797 nm, the reference signals and the subsequent signals 30 min after the cocaine injection were collected with noise-filtering and 0.8 mm spatial smoothing. Changes in HbT were calculated by $1+\Delta\text{HbT}/\text{HbT}$. On the B-scan image which showed the anatomical distribution of the HbT changes, positive HbT responses were used to indicate HbT increases between before and after cocaine injection.

3.3 Results and Discussion

PA B-scan images on coronal view of rat brain at two positions of 1.2 and 3.4 mm posterior to bregma were monitored throughout the experiment for imaging cortical functional changes. Figure 3.2 shows an example of the coronal view of a rat brain when 680 nm light wavelength was used. The result of PA B-scan images which are obtained from PAM system at bregma -1.2 mm and -3.4 mm are shown in Figure 3.3, respectively. The error bars showed in Figure 3.3 are the standard deviations of the measurements from four animals for PAM. According to the concentrations, the levels of changes are different; however, the signal intensities are increased gradually for 60 minutes. Figure 3.3 in common with Figure 2.3, shows higher concentration dose causes the higher increase.

The functional images (ΔI_F) show the changes of HbO₂ and Hb on cerebral cortex (Figure 3.4). The PA functional signals detected every 10 min after the injection of cocaine hydrochloride are shown. Because I_F is the ratio of PA imaging signals at 680 nm

to PA imaging signals at 797 nm, and at 680 nm, the optical absorption of Hb is dominant, a lower value of I_F means a lower concentration of Hb. Furthermore, a negative value in ΔI_F indicates the increase in sO_2 , and a positive value means the decrease in sO_2 . In Figure 3.4, the negative area becomes broader as time increases, indicating an increase in HbO_2 concentration. Meanwhile, Hb concentration decreased gradually until 30 min after injecting cocaine. This change in sO_2 indicates the activation of the rat brain after the injection of cocaine hydrochloride. As a result, the increase of blood oxygenation level after cocaine injection indicates the change in the rat brain, which is consistent with the higher sO_2 at 30 min than 10 min from previous studies (61, 62). Further, regions with the decreased sO_2 were also observed at 10 and 20 min. The result may suggest that there are regions experiencing decreases in sO_2 temporarily.

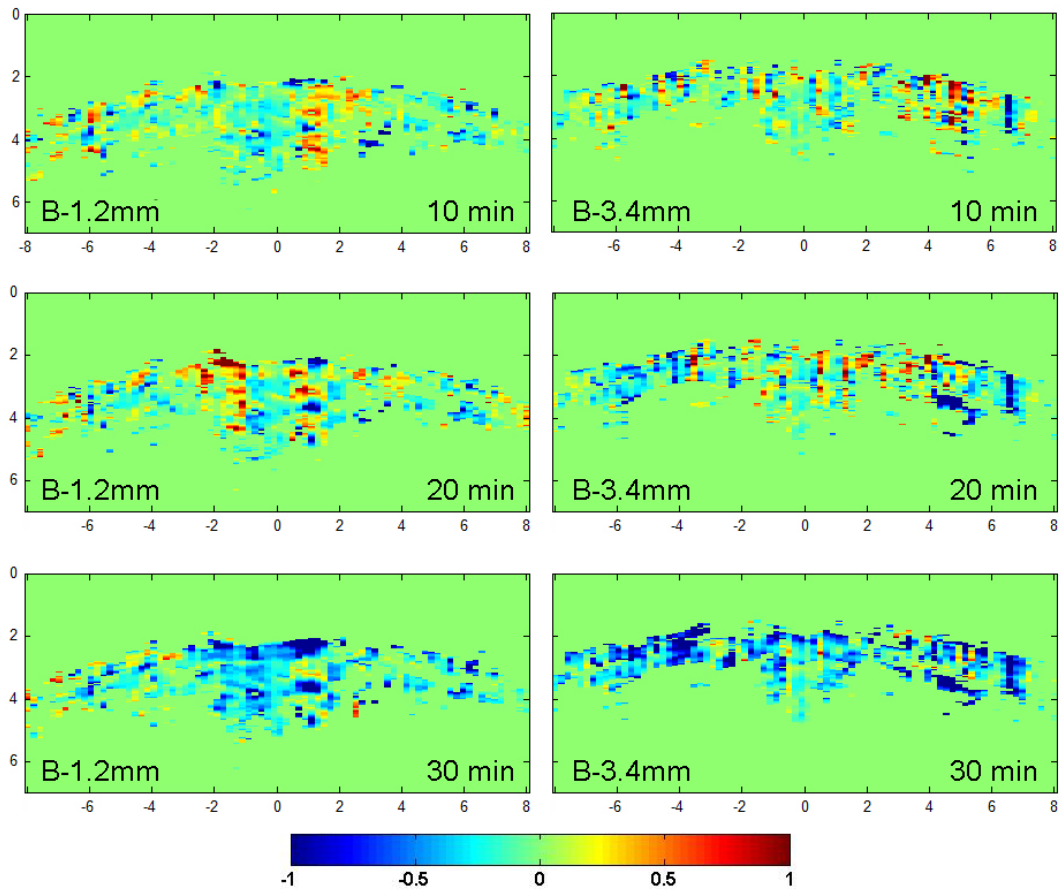


Figure 3.4 Functional images (ΔI_F) at 1.2 mm posterior to bregma, and 3.4 mm posterior to bregma. sO_2 changes are observed at 10, 20, and 30 min. The negative values in ΔI_F indicated the increases in sO_2 levels, and vice versa.

Figure 3.5 illustrates the percentage change in HbT concentration, and stereotaxic atlas reference lines are shown below the images for reference. We can confirm the increase in regional HbT concentration and the activated region in the rat brain cortex due to the effect of cocaine. The increase in HbT concentration is not uniform, with a maximum increase of 80% in some regions. From these results, we are able to identify the regional response of the brain to the injection of cocaine hydrochloride by identifying the anatomical region from stereotaxic atlas reference lines. A change in HbT implies a change in relative cerebral blood volume (rCBV). The conspicuous changes of rCBV on cortical layers have been shown by a previous study by Marota et al. with MRI (Ref. (63)) and the increase in rCBV was shown to be as high as 49% with a 1 mg/kg concentration of cocaine.

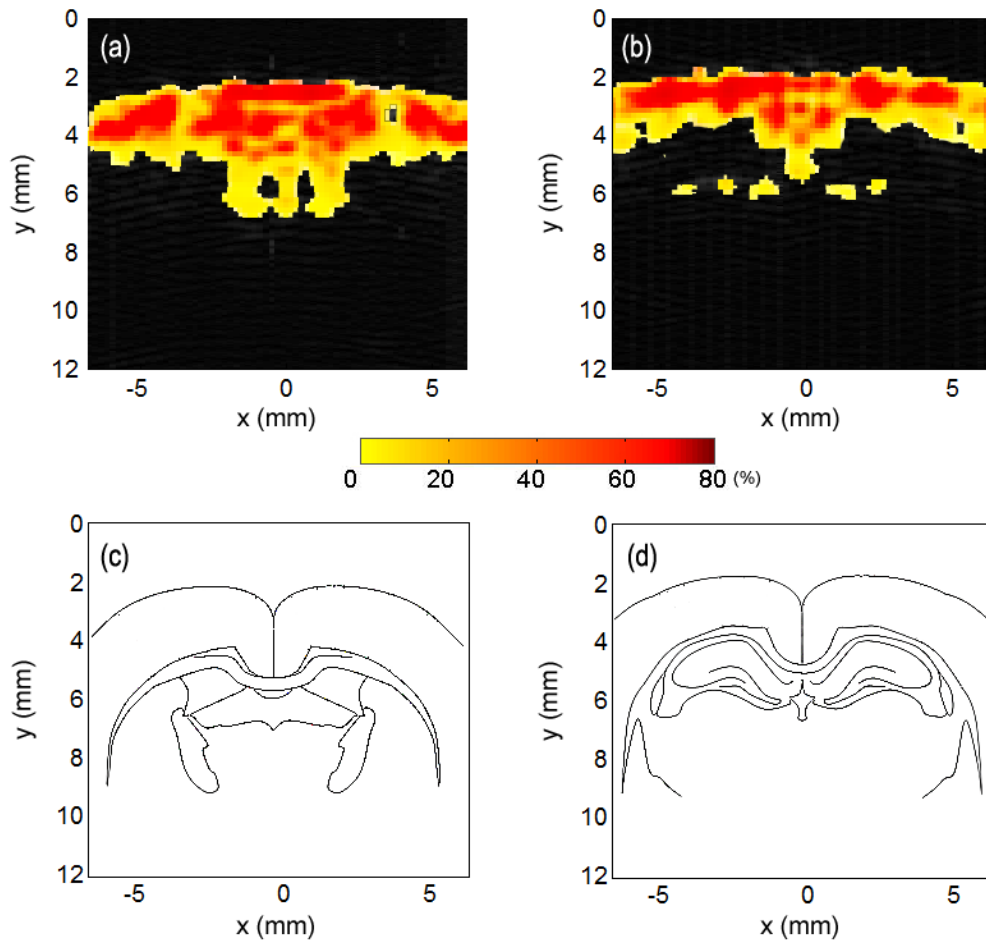


Figure 3.5 Photographs taken prior to (a), right after (b), 5 days after (c) and 16 days (d) after HIFU treatment. All photos are at the same length scale.

When PA imaging is used to detect brain activation, PA imaging does not directly measure changes in neuronal and glial signaling. Instead, PA imaging detects changes in hemodynamic activities, and normal neurovascular coupling is assumed. Although it is believed that blood flow and cell activities are coupled under normal conditions, recent

reports, however, described that neurovascular coupling may be compromised during progression of certain diseases or in response to certain drugs (64, 65). These results may limit the direct application of PA imaging on neuroimaging. A better solution may be to directly detect the metabolic rate by combining PA imaging and PA Doppler detection in the future.

3.4 Conclusions

After administration of cocaine hydrochloride injection, the rat brain activation was detected by scanning cerebral region with PA imaging methods. PA signal provides high signal-to-noise ratio images and probes in vivo functional changes in brain. The major advantage of the PA brain imaging is the combination of optical contrast and ultrasound resolution in deep regions. The ability of providing non-invasive brain functional imaging by PA imaging offers an important tool for small animal research. This research showed PA imaging is feasible for the study of brain activation due to drug abuse. As the verification for small animal, PA imaging has also demonstrated the ability of imaging for monkey, which may be thought this valuable technique is also used for human brain imaging in future.

PA imaging on coronal and transverse planes measures the changes in blood volume and the distribution of oxygenated hemoglobin in rat brain. However, due to the poor resolution of PAT imaging and limited ROI of PAM system for brain, current systems cannot detect wider area which covers most cortexes. To advance PA imaging,

modified PA imaging system can be designed, moreover, convenience and high performance may be improved for commercialization.

In summary, we used the PAM technique to monitor the pharmacological effect with photoacoustic functional detection in small animal brain in vivo. The regional change in HbT, which can be detected by PA imaging system effectively, was observed from the result of injecting cocaine hydrochloride. PA imaging on coronal view also shows the changes in the distribution of oxygenated hemoglobin in the rat brain. The results demonstrate that PA imaging can be used to monitor regional hemodynamic changes induced by drug abuse.

Chapter 4 Photoacoustic detection of functional responses in the motor cortex of awake behaving monkey during forelimb movement

4.1 Introduction

The spatiotemporal features of brain activation during various motor and cognitive tasks have emerged as an important research area in neuroscience over the past several decades. Numerous animal models have been used for this research. Non-human primates represent one of the best research models because of the high similarity between human and non-human primate brains (66-69). Functional magnetic resonance imaging (fMRI) has been used to detect functional changes in the primate brain, however, this technique is high cost and has poor temporal and spatial resolution when collecting functional information. Optical brain imaging, which can provide complementary information to fMRI and provide a low-cost alternative in many cases, has also been used to detect functional domains in the cortex of behaviorally active monkeys (70, 71). However, due to strong light scattering, high-resolution optical imaging can only monitor the surface of the exposed cortex, and depth information is very limited.

In this study, we applied PA imaging to detect activation of cortical areas in an awake monkey performing a reach and grasp task. PA imaging is based on the PA effect, and provides structural and functional images (72). During PA imaging, the light energy is absorbed by the tissue and converted into heat energy which causes the cells to expand instantaneously. Then, the ultrasound emission generated by the thermal expansion can be detected by an ultrasonic sensor. By using the detected ultrasound signals, PA images with ultrasound depth resolution and optical contrast are constructed. PA imaging can be

used to acquire functional information such as changes in the relative total concentration of hemoglobin (HbT), and the hemoglobin oxygen saturation (sO₂) (44, 55, 73, 74). In the brain, these hemodynamic changes can be related to the brain activity. Therefore, PA imaging can be used to detect task-related brain activation.

To the authors' knowledge, this study represents the first time that PA imaging has been applied to detect brain activation in an awake monkey associated with voluntary movements of the arm and hand. In our experiments, a customized PA imaging system was attached to a chronic recording chamber implanted over motor cortex of the left hemisphere. The system included a 20-MHz ultrasound transducer that was used to detect the hemodynamic changes in motor cortex during performance of a voluntary reaching task. Brain activation was monitored by detecting changes in regional total concentration of hemoglobin. This study demonstrates the feasibility to using functional PA imaging for brain research in non-human primates.

4.2 Materials and methods

For this study, a 9-kg, adult rhesus monkey (*Macaca mulatta*) was used. The monkey was seated in a custom built primate chair inside a sound-attenuating chamber. A reach-to-grasp task was performed with the right arm while the left forearm was restrained. The monkey initiated the task by placing its right hand on a pressure detecting plate located directly in front of the monkey at waist level. The monkey pressed the plate for 2-3 seconds after which a food pellet dropped into a small cylindrical food cup. The monkey then retrieved the food pellet with its right hand, carried the pellet to its mouth

and returned to the pressure plate to initiate a new trial. During continuous performance of this task the brain was scanned by PA imaging.

The monkey was first chair adapted and then trained on the reach-to-grasp task for several months. Once behavioral performance reached an acceptable level, an aseptic surgery was performed to implant a 30-mm inside diameter titanium chamber over the central sulcus at the level of forelimb primary motor cortex leaving the dura intact (69). The chamber was centered at anterior 16 mm, lateral and 18 mm lateral to the midline at an angle of 30° to the midsagittal plane. It was anchored to the skull with 12 titanium screws and dental acrylic. Figure 4.1 (a) and 4.1 (b) show the position of the chamber located. Figure 4.1(c) illustrates 3D MRI image and an enlarged view that shows the central sulcus (CS), arcuate sulcus (AS) and precentral dimple (PcD). The motor cortex between AS and CS is centered in the chamber. Figure 4.1(d) is a photo of a representative example of geometry around the CS from the paper published in 1997 by Gail Widener and Paul Cheney. This photo displays the cross-sectional depth of CS and intraparietal sulcus (IPS) of left brain. Surgeries were performed under isoflurane anesthesia and sterile conditions. Postoperatively, monkeys were given an analgesic (Buprenorphine 0.5 mg/kg every 12h for 3-4 days) and antibiotics (Penicillin G, Benzathaine / Procaine combination, 40,000 IU/kg every 3 days). All procedures were in accordance with the Association for Assessment and Accreditation of Laboratory Animal Care (AAALAC) and the Guide for the Care and Use of Laboratory Animals, published by the US Department of Health and Human Services and the National Institutes of Health. The study was approved by the University of Kansas Institutional Animal Care and Use Committees (IACUC).

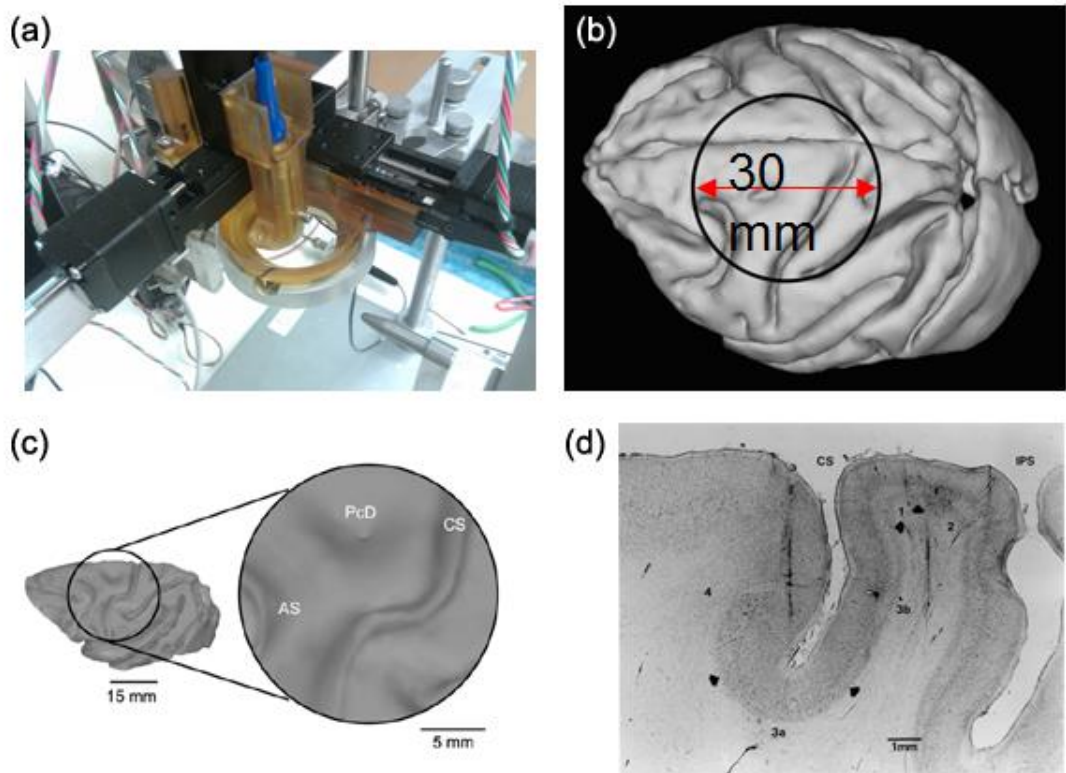


Figure 4.1 The imaging position. central sulcus (CS), arcuate sulcus (AS) and the precentral dimple (PcD). (a) Motorized scanner (b) The position of the cortical chamber on the monkey brain (c) 3D MRI image and enlarged view of the revealed within the chamber (d) a photo of a representative example of geometry from the paper published in 1997 by Gail Widener and Paul Cheney.

A schematic of the PA imaging system with the chamber on the monkey's head is shown in Figure 4.2. During imaging process, the cover of the chamber was removed to expose dural surface, and saline solution was used to fill the chamber. The detection surface of PA detector was then immersed in saline solution. The illumination light source was a Q-switched 30-Hz pulsed Nd:YAG laser (Surelite OPO PLUS; Continuum, Santa Clara, CA) producing light at 532 nm wavelength. The light was delivered through an optical fiber to the dural surface overlying motor cortex. The incident energy density of the laser that reached the dural surface was less than 5 mJ/cm^2 , which complies with the safety limit for human skin exposure.⁽⁴⁵⁾ The PA signal from the cortex was collected with a 20-MHz focused ultrasound transducer (V316, focal distance: 0.5 inch, Olympus-NDT, Waltham, MA). The detected PA signal was amplified (5072PR, Olympus-NDT, Waltham, MA) and collected using a data acquisition board (CS21G8, Gage, Lockport, IL). Two automated stepper motors (Figure 4.1) were used to allow 2D scanning of the brain. The scanning step size was $100 \text{ }\mu\text{m}$ for both directions in the scanning area. A third manual translation stage was used to adjust the height of the sensor and laser source above the dural surface. At each scan position, A-line data (2000 samples, 250 MHz sampling rate) was acquired.

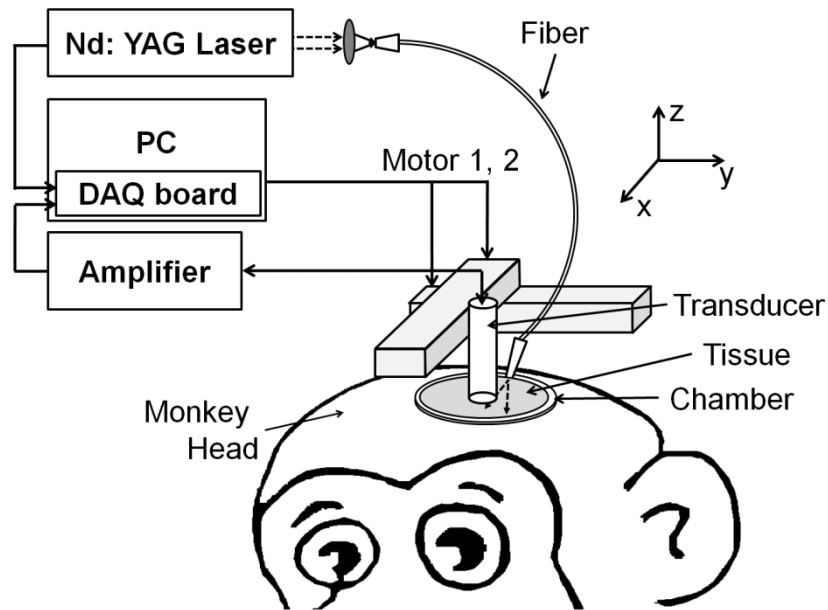


Figure 4.2 Time sequence of data acquisition and HIFU waves.

In each imaging session, the PA sensor scanned a 16×8 mm ovoid-shaped region inside the cranial chamber using the computer controlled two-axis motorized stage. A reference image with the behavioral task off was always obtained first. Then, the same brain area was scanned while the monkey performed the reach-to-grasp task with its right arm/hand. It took 7 minutes for each scanning. The PA data were acquired continuously during the task-off for about 15 minutes to get two reference images for averaging. Then the monkey performed the same task repeatedly for about 15 minutes and another two PA images were taken for averaging during this process. Since the experiment used 532-nm

laser light, which is an isospectral point of hemoglobin absorption, the amplitude of the detected PA signal was proportional to the concentration of total hemoglobin. Therefore, an increase in imaging intensity indicated an increase in the concentration of total hemoglobin.

4.3 Results

The region of interest in the left hemisphere is shown in Figure 4.3. Figure 4.3(a) is the reference image obtained with the behavioral task off, and Figure 4.3(b) is the image acquired when the monkey was performing the reach-to-grasp task with the contralateral arm. The two images (Figures 4.3(a) and 4.3(b)) are maximum-amplitude-projection (MAP) PA images, where the maximal amplitudes of detected PA signals along the depth direction are projected to the imaging plane. Comparing Figures 4.3(a) and 4.3(b), regional changes in the amplitude of PA signals can be observed. These regional changes indicate changes in brain activity associated with task performance. Primary motor cortex (M1) is activated in association with motor execution and primary somatosensory cortex (SI) is activated in association with stimulation of various sensory receptors by the movement itself and also by grasping the food pellet. An overlay of the PA image and the MRI structural image is shown in Figure 4.3(c). From the MRI image, M1 and SI cortex can easily be identified. The average increases in PA signal amplitude in M1 and SI cortex during movement compared to the task off condition are given in Figure 4.3(d). The PA signal amplitude increased 28 % in M1 and 27% in SI compared to the task off condition. These results were averaged over the area indicated by the dotted

lines in Figure 4.3(a) and 4.3(b). Note that the area encompassed by the dotted line is largely M1 but includes a small part of premotor cortex anteriorly. An increase in the signal amplitude indicates an increase in total hemoglobin concentration. Increased total hemoglobin concentration is associated with increased blood flow related to the additional energy requirement of increased neuronal activity.

The task off condition shows activation of a region that is largely within the M1 representation although it has a different spatial localization than the activation observed during actual task performance. The origin of the signal during the task off condition is not clear. The monkey was largely at rest but over the period of 7 minutes required for the scan there were small movements or isometric contractions or low level muscle activation that would not be readily observable. It is also possible that even though the task was off, the monkey might have been anticipating a return to active task performance and the activation observed in this condition was related to anticipation.

Depth-resolved images are shown in Figures 4.3(e) and 4.3(f). PA B-mode images are overlaid on a parasagittal section taken from the reconstructed MRI of the brain. The structural MRI image shows a cross-section through the AS and CS at the level marked by the black line in Figures 4.3(a) and 4.3(b). Figure 4.3(e) is a reference image acquired with the monkey at rest and Figure 4.3(f) is the image acquired from the same location during performance of the reach-to-grasp task. During performance of the reaching task, PA signal amplitude in motor cortex anterior to the CS increased. In this image, average PA signal amplitude in M1 increased by 45.8% and by 35% in SI. The level shown in the figure was selected because it encompassed an area of motor cortex that was relatively

quiet in the task off condition but activated during active task performance. Clearly, the specific increase observed will depend on the level of the parasagittal section.

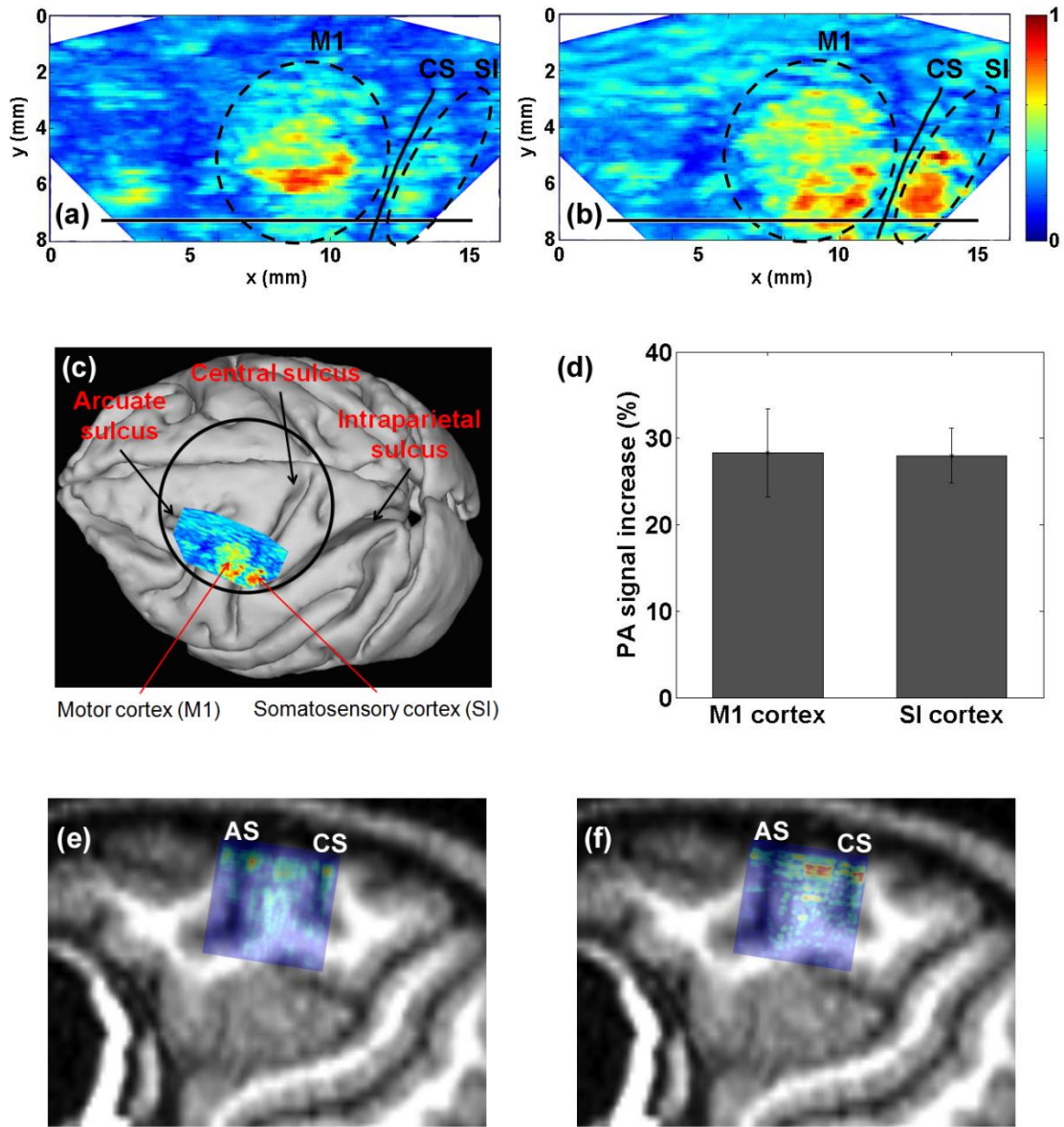


Figure 4.3 PA images of functional activity in primary motor cortex and primary somatosensory cortex of a macaque monkey. Color scale indicates the amplitude of the detected PA signal with “1” indicating the maximal value. (a) Reference image acquired with the behavioral task off. Primary motor cortex (M1), primary somatosensory cortex (SI) and the location of the central sulcus (CS) are identified. (b) Image obtained over the same region of the cortex while the monkey was performing a reach-to-grasp task with its contralateral forelimb. (c) Overlay of the PA image obtained during movement on an MRI image of the monkey’s brain. The dark line circle shows the position of the rim of the cranial chamber. (d) Changes in the average PA signal obtained from M1 and SI cortex averaged over the regions outlined by the dotted lines in (a) and (b). Note that the area encompassed by the dotted line is largely M1 but includes a small part of premotor cortex anteriorly. (e) PA B-mode functional image superimposed on an MRI cross-section through the central sulcus. The black line in Figure 4.3(a) shows the location and orientation of the section. The B-mode image was acquired with the task off. The dimension of the PA image is 12 x 12 mm. (f) The same image as (e) but obtained during performance of the reach-to-grasp task.

4.4 Discussion and Conclusions

The images showed are averaged images obtained on the same day within one hour. We have also performed the experiment in different days and observed similar results, which further confirmed the feasibility of the technique. Several problems have to be overcome in applying PA imaging to the awake monkey performing a behavioral task. Motion artifacts due to the head movement of the monkey induce blurring of PA images. To maintain comfort of the monkey, our head fixation system was not totally rigid but allowed small movements in all directions. These movements may induce motion artifacts and reduce the spatial resolution. These artifacts were largely eliminated by designing an adaptor for the scanning device that attached directly to the recording chamber implanted on the monkey's skull. In addition, because the recording sessions were time restricted, the numbers of scans for averaging were also limited.

In the future, an important improvement in our approach could be achieved by using an ultrasonic array transducer. Using a multi-channel system would reduce scanning time and provide quantitative data for various functional images in real-time. Real-time imaging will provide excellent temporal resolution and significantly reduce motion artifacts caused by monkey head movement. In addition, another future work would be using multiple laser wavelengths to measure blood oxygenation saturation in the brain,(43) and it should allow us to gain more information about the brain functions.

Another possible future improvement will be performing transcranial PA imaging of monkey brain. Several research results have shown the feasibility of transcranial PA imaging for monkey brain (48, 75, 76). At current stage, the imaging resolution and

imaging depth is still limited because of the skull effect. However, as more advances algorithms become available, the above mentioned limitations could be resolved.

In conclusion, we have shown that PA imaging can be used for mapping brain functional activity in awake, behaviorally performing monkeys. PA imaging detects changes in hemodynamics associated with neuronal activation within the brain. We have demonstrated activation of primary motor cortex and primary somatosensory cortex during performance of a task involving reaching and grasping using the contralateral forelimb. Our results establish the feasibility of using PA imaging as a valid method for identifying and mapping task related areas of cortical activation in non-human primates.

Chapter 5 The propagation of photoacoustic shock wave

5.1 Introduction

Photoacoustic (PA) imaging modality has been used for various biomedical researches such as tumor angiogenesis detection, hemodynamic monitoring, functional brain imaging, and sentinel lymph nodes mapping (77-80). PA imaging modality combines the resolution of ultrasound imaging and contrast of optical imaging (1, 72). Photoacoustic effect is based on physical mechanism of generation of acoustic waves by the absorption of optical energy. When nonionizing light source such as short laser pulses illuminates a sample tissue, the absorbed light energy generates a pressure perturbation due to instantaneous thermal expansion, and the pressure perturbation propagates as an acoustic wave at a certain speed, amplitude and direction. Once detected, the acoustic signal can be used to reconstruct images in a 3-dimensional (3D) space.

For the excitation source of PA imaging, nonionizing light with a wavelength ranging from the visible part of the spectrum (400~700 nm) to the near infrared (700~1100 nm) is employed. Unlike other optical imaging modalities, the resolution of PA imaging is not affected much by the scattering of photons. PA imaging detects the acoustic signals generated by the absorbed photons by using ultrasound transducers with center frequencies ranging from 1 to 50 MHz. Therefore, PA imaging can provide good spatial resolution because ultrasound scattering in tissue is two to three orders of magnitude weaker than optical scattering (6).

Recently, many studies have been carried out to develop algorithms for quantitative PA image reconstruction (81, 82). Quantitative PA imaging can provide accurate information regarding local tissue properties, resulting in much more sensitive detections. To accurately reconstruct PA images quantitatively, the energy dissipation mechanisms, including both optical and acoustical, must be considered. For PA wave propagation, linear acoustic model has been used to provide simple analysis of pressure waves. Some recent works (83, 84) have included the effect of acoustic attenuation in the image reconstruction algorithm. However, PA waves generated by the short pulsed laser are shock waves by nature (85). Therefore, to accurately model the propagation of PA waves, the propagation of shock waves must also be considered. So far, only few studies considered the generation and propagation of shock waves during the propagation of PA waves(86, 87), and the effect of shock wave–related energy dissipation mechanism on PA wave propagation has not yet been studied.

Because the pulse of optical source used in pulse-mode PA imaging is short enough to generate sudden expansion and contraction due to the thermoelastic nature of tissue, the change in stress, density and temperature at the irradiation site occurs quickly. This rapid change makes the PA wavefronts vary differently according to the strength of pressure waves, and can be interpreted as shock waves that dissipate differently from an ordinary wave. This study will use solutions of shock wave theory to obtain the solution of nonlinear PA propagation. In addition, the difference between linear solution and nonlinear solution will be shown with simulations of spherical waves. This study can provide different perspectives for the propagation of PA waves and consideration for more accurate energy loss during quantitatively PA imaging.

5.2 Methods

5.2.1 Linear solution

The amplitude of PA wave depends on the duration of the laser pulses. In the case of short laser pulse, PA wave generation is regarded as stress confinement. Without consideration of the influence of heat conduction and attenuation of sound, the PA wave generation and propagation in an inviscid medium is described by the general equation,

$$\nabla^2 p - \frac{1}{c_0^2} \frac{\partial^2 p}{\partial t^2} = -\frac{\beta}{c_p} \frac{\partial H}{\partial t}, \quad (1)$$

where β represents the thermal expansion coefficient, C_p is the specific heat at constant pressure, and H is the heating function defined as the thermal energy converted per unit volume and time (88). The linear solution for the propagation of PA wave from a spherical target shows an N-wave form. From Eq. (1), the linear solution for spherical wave can be obtained (4, 89). When radius of the sphere is r_0 , an initial pressure p_0 is generated inside the sphere that is heated up with a delta pulse. If the observation point is outside the sphere ($r > r_0$), three cases are considered according to the propagation time. And we can have (4, 89)

$$p(r, t) = \frac{r+v_s t}{2r} p_0(r + v_s t) + \frac{r-v_s t}{2r} p_0(-r + v_s t) + \frac{r-v_s t}{2r} p_0(r - v_s t). \quad (2)$$

The pressure is composed of three terms which represents a converging spherical wave, a diverging rarefaction spherical wave converted from the initially converging wave propagating through the center, and a diverging spherical wave. Depending on the observation point, the waveform of the linear Eq. (2) changes as Figure 5.1. Figure 5.1 shows the propagated photoacoustic wave from spherical target of 1 mm radius on the distance of once, twice, and three times of the radius from the target when only linear theory is considered.

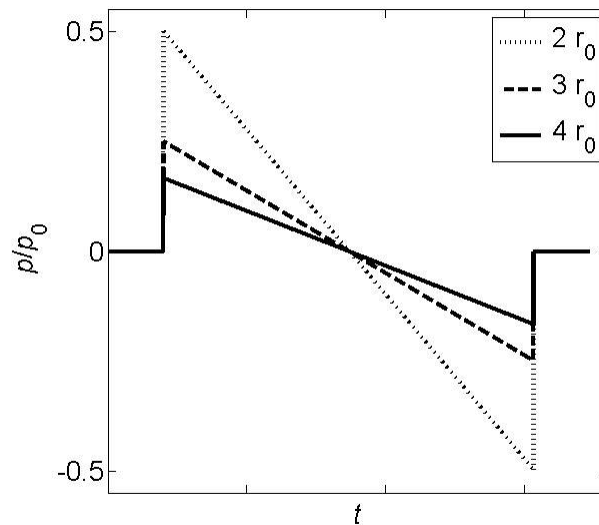


Figure 5.1 Changes of the linear propagating spherical waveforms generated from sphere target on the different distances.

5.2.1 Nonlinear solution

The basic general relations for the propagation of simple waves were discovered by Poisson, Stokes, DeMorgan and Airy and Earnshaw (90). The theory of shock waves was given a basic form by Rankine-Hugoniot shock relations. The shock wave solution in this study was based on Hugoniot's shock relation combining Earnshaw solution with Poisson solution (91). From the propagation of plane progressive wave in a fluid, the propagation model that relies on the Earnshaw solution to weak shock theory may be written as

$$p = f(\phi), \quad \phi = \tau + \frac{\beta x f(\phi)}{\rho_0 c_0^3} \quad (3)$$

where x is the distance from the source, β is the coefficient of nonlinearity, ρ_0 is the ambient density, τ is the retarded time ($t - x/c_0$), and c_0 is small-signal sound speed (91, 92). The waveforms obtained from Eq. (3) show theoretical formulation. The waveforms may deform as it propagates over a relative long distance due to nonlinearity. The waveform deformation can generate a triple-valued waveform, after the wave becomes the shock wave. However, a waveform cannot have the triple-valued state actually (91). The forward phase that travels faster toward x direction balances the opposite phase left behind. To reach the suitable formulation for empirical observation, we use Equal Area Rule (EAR) with which the shock arrival time t_{sh} is denoted between triple-valued area. The shock waves have different propagation velocities in the waves before and behind

the shock. Earnshaw solution as Eq. (3) can be expressed with p_a and p_b for before and behind of shock. The shock wave with EAR is,

$$\tau = f^{-1}(p_a) - \frac{\beta x p_a}{\rho_0 c_0^3} \quad (4)$$

$$\tau = f^{-1}(p_b) - \frac{\beta x p_b}{\rho_0 c_0^3} \quad (5)$$

where f^{-1} is the inverse function corresponding to f (93). Figure 5.2 shows the shock waveform and decay as the distance x increases. The dashed line and solid line display the theoretical waveform and shock wave with equal-area rule applied, respectively. After distortion of the wave, the curves of the wave become sharp and the shock amplitude continues to decline.

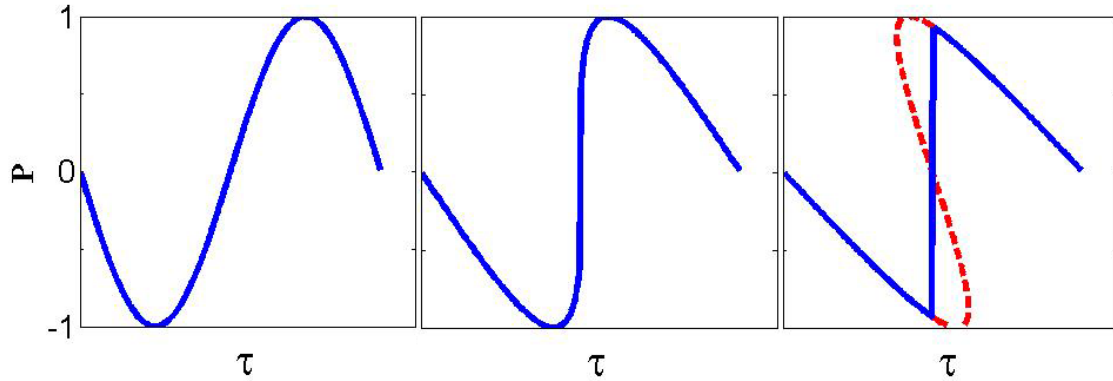


Figure 5.2 Distortion of propagating plane shock waveforms. Dashed line displays theoretical waveform. Solid line is the waveform with equal-area rule applied (the actual waveform). The amplitude of pressure is normalized by the initial pressure (p/p_0).

To describe a shock wave solution for PA waveform transforming during propagation, the wave solution should be considered on three-dimension. Here the shock wave for spherical wave begins from the generalized Burgers equations (94, 95),

$$\frac{\partial p}{\partial r} + p \frac{m}{r} = \frac{\beta p}{\rho_0 c_0^3} \frac{\partial p}{\partial \tau} \quad (6)$$

where $m = 1$ for spherical waves, r is the radial coordinate, and $\tau = t \mp (r - r_0)/c_0$ for both diverging and converging waves. When the pressure $q = (r/r_0)p$ with the source radius r_0 , and the distance $z = \pm r_0 \ln(r/r_0)$ replace p and x respectively. With $\frac{dz}{dr} = \pm \left(\frac{r_0}{r}\right)^m$, Eq. (6) becomes,

$$\frac{\partial q}{\partial z} = \frac{\beta q}{\rho_0 c_0^3} \frac{\partial q}{\partial \tau}. \quad (7)$$

The corresponding solution for a spherical wave with source condition $p = f(t)$ at $r = r_0$ is (91),

$$p(r, \tau) = \frac{r_0}{r} f(\Phi), \quad \Phi = \tau \pm \frac{\beta p r}{\rho_0 c_0^3} \ln \frac{r}{r_0}. \quad (8)$$

In this study, both plane and spherical shock wave solution (Eq. 3 and 8) will be applied to simulate the propagation of PA waves. The effect of nonlinearity of during PA wave propagation will be analyzed.

5.3 Results and Discussion

5.3.1 Nonlinear propagation of PA waves

The shock wave solution was applied to PA wave propagation from a spherical target, which starts with an N wave. In Figure 5.3, we can see the wave distortion during propagation. Figure 5.3(a), 5.3(b), and 5.3(c) show the distortion of N-waveform with plane shock wave solution in Eq. (3), while Figure 5.3(d), 5.3(e), and 5.3(f) show the waveform change using the spherical shock wave solution in Eq. (8). Figure 5.3(a) and 5.3(d) shows the waveform on the propagation distance r_0 . The examples in Figure 5.3(b) and 5.3(e) show the waveform on propagation distance $2r_0$, and Figure 5.3(c) and 5.3(f) on $3r_0$. The dotted line displays the theoretical waveform of distorted N-wave. The solid line is the waveform that is applied to EAR. The propagating photoacoustic wave has N-shaped waveform with different amplitude changes of pressure. In these examples, to emphasize the effect of nonlinearity, we chose the initial pressure, size of target sphere, and observation distance that can clear demonstrate the effect of nonlinear effect. The effect of nonlinearity largely depends on these parameters.

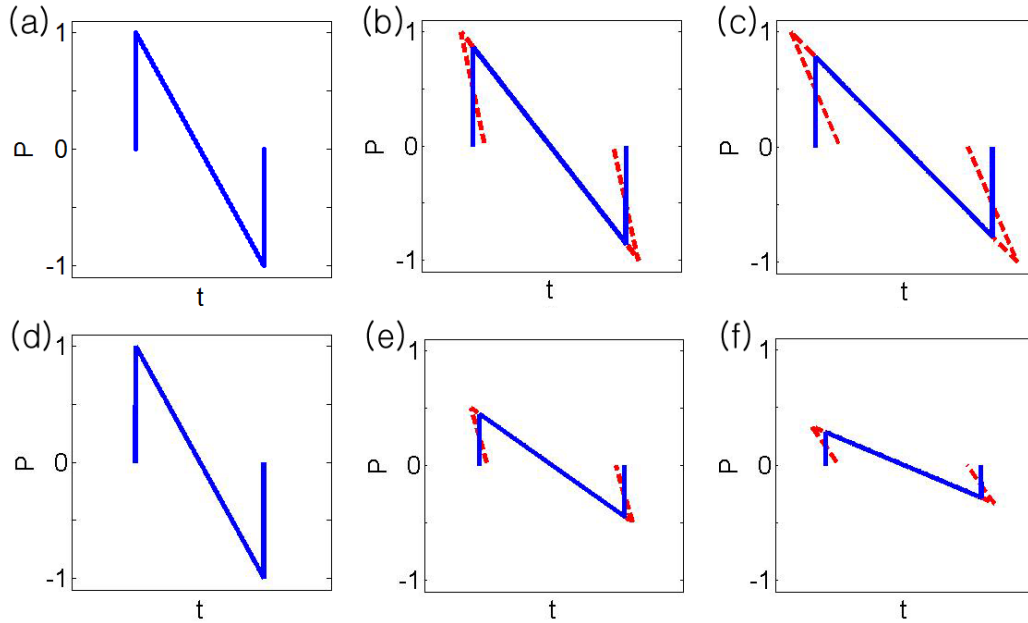


Figure 5.3 Change of N-waveform applied the shock wave solution for plane wave (a~c) and spherical wave (d~f). The dotted line and the solid line indicate the distorted photoacoustic wave and the shock wave with equal-area rule (the actual waveform).

To compare linear photoacoustic wave propagation and nonlinear solutions, the same of initial pressure, size of target sphere, and observation distance were used. Figure 5.4 shows the difference between the linear solution and the shock wave solution for a spherical wave. The propagating spherical waves on the distances of r_0 , $1.5r_0$, $2r_0$, and $2.5r_0$ show the obvious differences between the spherical wave solutions. We used experimental values for PA imaging to simulate and compare the propagation of spherical waves in linear and nonlinear solution.

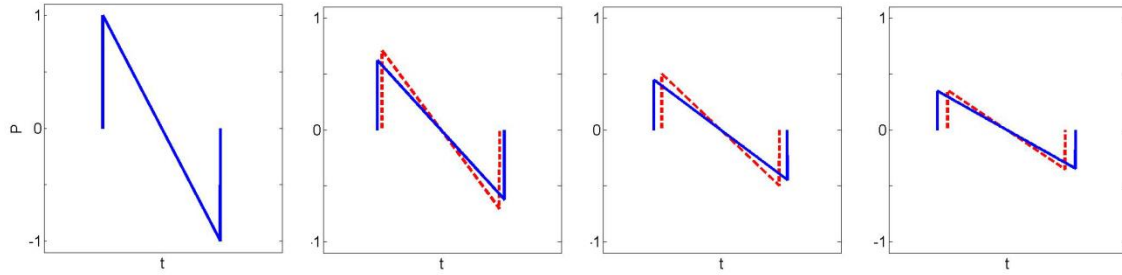


Figure 5.4 The propagating PA spherical waves on the different distance. The dashed line indicates the linear spherical wave, and the solid line indicates spherical shock wave.

5.3.2 Comparison between linear and shock wave solutions

In this part of simulation, we assumed the surrounding media for PA propagation was water. Since the attenuation coefficient of water is small, the effect of acoustic attenuation is neglected. The shock effect is strongly related to the amplitude of the propagating wave. Therefore, we need to estimate the initial PA signal amplitude. Figure 5.5 shows the PA signal generated from a black hair using 532 nm wavelength laser light and 20 mJ/cm^2 fluence. The signal was detected by a standard needle hydrophone (1462, Precision Acoustics LTD, UK) at 20-mm distance. The amplitude of the signal was 4.2 mV that is equal to 10.9 kPa at 10 MHz, which is the center frequency of the signal. By assuming only spherical spreading during the propagation, the initial pressure at 150- μm distance, which is one wavelength (at 10 MHz) away from the source, can be estimated to be $\sim 1.17 \text{ MPa}$. Therefore, the initial PA amplitude was set at 1 MPa in the following simulations.

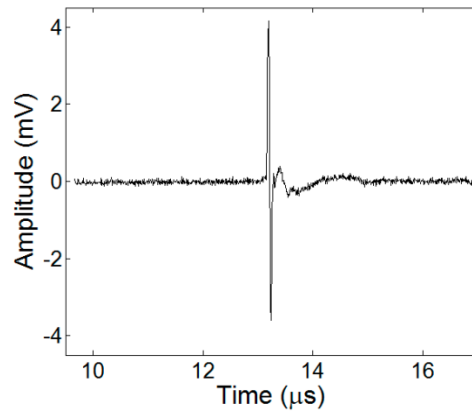


Figure 5.5 Photoacoustic signal from a black hair detected by a standard needle hydrophone. The peak amplitude is equal to 1.17 MPa at 10 MHz, which is the center frequency of the signal.

For simulation of spherical PA wave propagation, we assumed water density was $1,000 \text{ kg/m}^3$ and sound speed was $1,484 \text{ m/s}$. The coefficient of nonlinearity β that is $1+B/2A$ was 3.5 in water, the radius of sphere target was $150\text{-}\mu\text{m}$, and the initial photoacoustic pressure 1 MPa estimated based on the result of Figure 5.5. The results of amplitude changes as a function of propagation distance were shown in Figure 5.6(a). The amplitude of the spherical wave dropped very quickly when shock wave effect was considered. Figure 5.6(b) shows the relative error between the amplitude of the linear and non-linear spherical wave solution. Note that the dispersion of shock wave was not considered in these simulations.

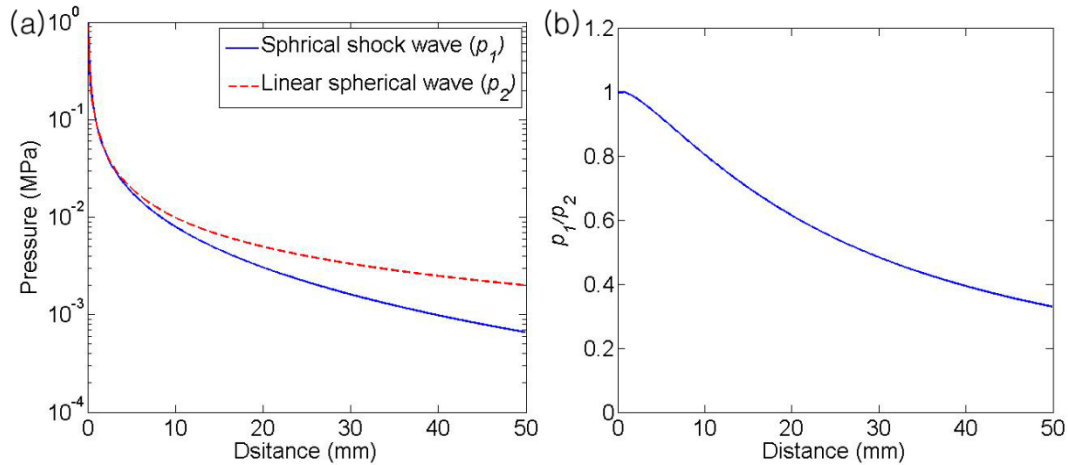


Figure 5.6 Comparison of the peak amplitude of the pressure between linear and nonlinear spherical wave models. (a) Pressure amplitude, and (b) ratio between nonlinear and linear solution

The shock distortion can be continued while the wave propagates. The relative error that was calculated by the ratio of the amplitude of the pressure between the two lines in Figure 5.6 increased as the wave propagated. Figure 5.7(a) shows the relative errors for 500 μm , 750 μm , and 1 mm of the target radii. The error decreased when the radius of target sphere was bigger. The effect of different initial pressures is shown in Figure 5.7(b) where 0.5 MPa, 0.75 MPa, and 1 MPa were used for the initial pressures. The error between spherical waves decreased when the initial pressure decreased. These results indicate the effect of nonlinear wave propagation is closely related to the size of the target and the initial PA wave pressure.

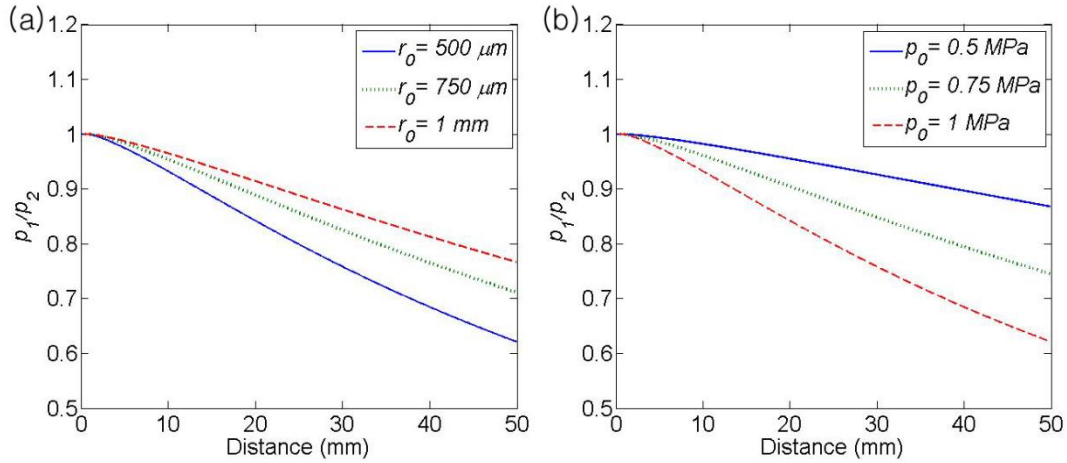


Figure 5.7 The relative error between the amplitude of the linear and non-linear spherical wave solution with (a) different radii of target sphere, and (b) different initial pressures.

This study only considered the effect of nonlinearity, and showed considerable differences between nonlinear and linear PA wave propagation. In human soft tissue, however, the effect of shock wave propagation can be limited by the strong acoustic absorption when the wave propagates over a relatively long distance. The combined effect of nonlinearity and acoustic absorption, therefore, need further investigation in the future.

5.4 Conclusions

PA imaging employs pulsed laser light that is enough to create weak shock wave. In this study, the shock wave solution was introduced to investigate PA wave propagation. We used N-waveform of initial PA wave from a sphere. The wave distortion that is

applied to shock wave theory was shown and compared with linear spherical wave solution. This study presents the decrement of PA waveform with the nonlinear solution of spherical wave. With the results, we can estimate shock distortion is closely related to the initial PA pressure and target size. Also, the results show the large variation of the relative errors in the range of real PA pressure amplitude. The wave propagation considering shock wave will provide more accurate information for quantitatively reconstructing photoacoustic images.

Chapter 6 Laser-enhanced high-intensity focused ultrasound heating in an *in vivo* small animal model

6.1 Introduction

Ultrasound waves are mechanical vibrations above the threshold of human hearing (20kHz). These oscillating pressure waves can be used for detecting objects, measuring distances, non-invasive imaging, cleaning, mixing, and accelerating chemical processes in various fields. Particularly, it has been widely used in the clinic for diagnostic sonography which usually uses frequencies in the range of 1-20 MHz. In addition, therapeutic ultrasound, such as high-intensity focused ultrasound (HIFU) in frequencies of 0.5-5 MHz, can be used to locally destroy diseased tissues.

HIFU is a non-invasive procedure that works through rapidly depositing high intensity ultrasound energy into a small region to induce cell necrosis primarily by hyperthermia (27, 28, 96). Since the first publication for potential applications of HIFU in 1942, the investigations of HIFU have continued for several decades (30). Recently, HIFU technique has been used in the treatment of various conditions such as uterine fibroids, particular solid tumors, atrial fibrillation, and functional neuro surgery (97-101). The number of HIFU applications has increased rapidly and the clinical technique has been developed in combining with advanced medical imaging modalities. These medical imaging modalities include ultrasound imaging, magnetic resonance imaging (MRI) and computed tomography (CT). These techniques offer advantages for therapy planning, monitoring and visualization of the target during HIFU. Under imaging guidance, HIFU transducers deliver ultrasound energy to the focal region with intensities in the range of

100-10,000 W/cm², which are corresponding to peak pressures of up to 30 MPa. The high acoustic intensities in tissue cause heat generation due to absorption of the acoustic energy. This heat generation can increase the tissue temperature to more than 80°C in the tissue, and coagulation necrosis can occur in a few seconds (102).

In company with the thermal effects, mechanical phenomena such as cavitation, microstreaming, and radiation forces arise from high intensity ultrasound (98). Acoustic cavitation that is the creation or motion of a vapor cavity occurs due to alternating compression and expansion of tissue and the elevated tissue temperature. The rapid expansion and collapse of the cavitation bubbles generates high instantaneous pressures that can cause physical damage and enhanced heating effects, which can improve the efficiency of HIFU treatment (103-106). The enhanced heating by cavitation refers to extra heat generation that is over the heat caused by classical thermoviscous absorption of the ultrasound energy. The additional heat generation can be explained by viscous damping from cavitation radial motion and local absorption of the acoustic emissions from inertial cavitation collapses (103, 104, 107, 108). Broadband acoustic emissions are correlated with cavitation activities and have been used as an indicator to detect cavitation during HIFU. Experimentally, the broadband acoustic emission can be detected by passive cavitation detector (PCD) (109-111).

Previously, we studied photoacoustic imaging (PAI)-guided HIFU therapy. PAI is a hybrid imaging technique that maps acoustic signals resulting from thermo-elastic expansions due to the absorption of laser light by biological tissue (12, 16, 40, 44). During PAI-guided HIFU therapy, laser light was employed to illuminate the target

concurrently with HIFU radiation. We reported that the concurrent use of PAI during HIFU therapy can result in enhanced cavitation activities, and therefore, elevated temperature rise (109, 112, 113). Unlike other studies, these results demonstrated a particle-free, laser-enhanced HIFU heating method with a diagnostic laser system, where the laser fluence is relatively low and direct inductions of cavitation by laser alone is unlikely. Results from these investigations strongly suggested that enhancing cavitation and heating by combining laser exposure and HIFU is feasible.

In the current study, we further investigate the enhanced heating effect when a diagnostic laser system is used concurrently with HIFU in an *in vivo* animal model. Laser light, whose intensity is limited by the safety standard recommended by American National Standards Institute (45), is used to illuminate the thighs of murine animals during HIFU treatment. The enhanced cavitation activity and temperature rise are monitored by a passive cavitation detector (PCD) and a thermocouple. In addition, the potential mechanisms for the enhanced cavitation activity during concurrent use of laser and HIFU are discussed.

6.2 Methods

6.2.1 Experiment setup

The experiment procedure consisted of imaging the HIFU region, measuring temperature by a thermocouple during HIFU treatments with and without laser light, and detecting cavitation signals by a PCD. A combined PAI and HIFU system (58, 114, 115)

was employed to provide the imaging capability and laser illumination during HIFU treatment. The temperature was measured with the thermocouple embedded in an *in vivo* small animal's thigh. The positions of HIFU target regions with and without laser were determined by 2D or 3D images of the targeted areas from PAI. The experiment was implemented under different conditions of HIFU pressures, wavelengths of laser, and HIFU lesion depths. Under each condition, the temperature rises and cavitation signals were collected and compared for both cases of HIFU with and without laser illumination.

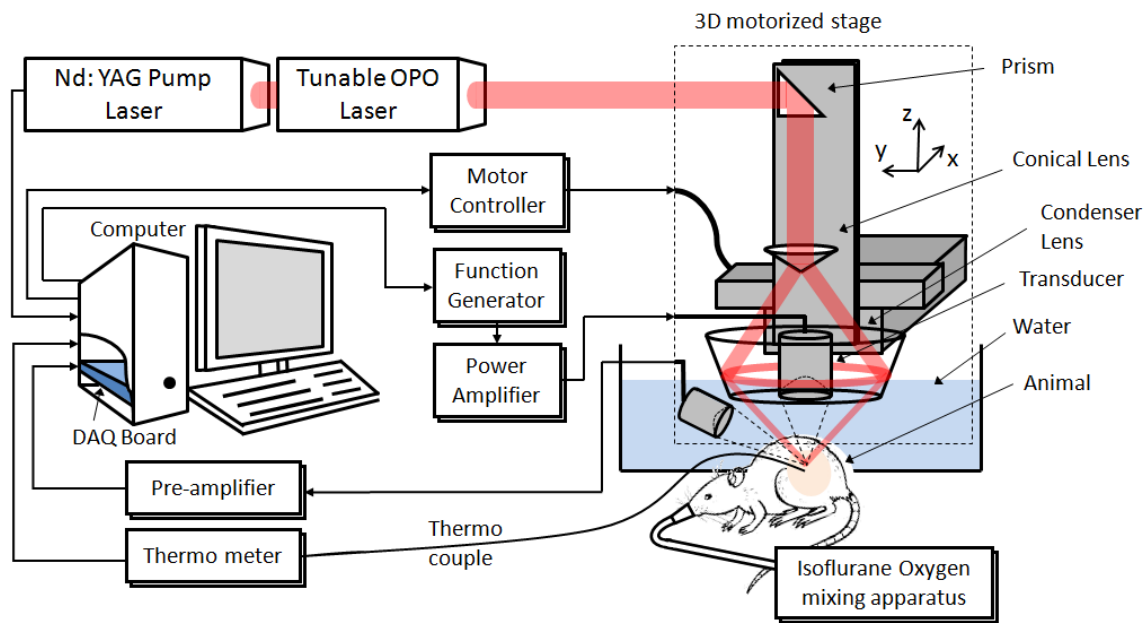


Figure 6.1 Schematic of the PAI-guided HIFU system.

Figure 6.1 shows the detailed schematic of the system. A tunable optical parameter oscillator (OPO) laser (Surelite OPO PLUS, Continuum, Santa Clara, CA)

pumped by a Q-switched, Nd:YAG laser with a pulse repetition rate 10 HZ (~5-ns pulse width) was used for the laser light source. The laser light was delivered by a couple of prisms and a conical lens to form a ring-shaped illumination pattern. The laser beam was then focused by the condenser lens to make the laser beam confocal with the focus of a 5 MHz transducer (SU-108-013, Sonic Concepts, Bothell, WA). The 5 MHz transducer (35 mm focal length and 33 mm aperture size) was located in the center of the condenser lens and used for both HIFU and PAI purposes. A 10 MHz focused ultrasound transducer (V315, Olympus NDT, MA) that had a 37.5 mm focal length was used as a PCD. The PCD transducer was located where the focus of the PCD overlapped the focuses of the HIFU transducer and laser beam.

6.2.2 Animal model

In this study, we used mice (BALB/c, 15-20 g, female) and rats (Sprague Dawley, 200-250 g, female) for the *in vivo* experiments. All animals were handled and cared for in accordance with the Guide for the Care and Use of Laboratory Animals, and the procedures were approved by the Institutional Animal Care and Use Committee at the University of Kansas. For an experiment, an animal was initially anesthetized with a mixture of ketamine (87 mg/kg body weight) and xylazine (13 mg/kg body weight), and the inhalational anesthesia with 1.0-2.0 % of isoflurane mixing in pure oxygen was used to maintain the subsequent anesthesia. After shaving of the hairs on the animal thigh with an electric shaver and standard surgical hair removal lotion, the animal was maintained under anesthesia for at least 1 hour to reach equilibrium body condition. Then, the anesthetized animal was fixed on a custom-designed animal holder and the body temperature was maintained with a water circulating pad. To measure temperature in the

region, a 50- μm diameter, T-type thermocouple was inserted into the animal leg region through a needle. The location of the thermocouples is visualized by PAI to place the HIFU implement location 0.2 mm away from the thermocouples tip. The animal was coated with ultrasound gel and placed under the acoustic coupling membrane in a water tank filled with degassed water. During PAI and HIFU implementation, the heartbeat and blood oxygenation of the animal were monitored with a pulse-oximeter.

6.2.3 Experiment procedure

During HIFU treatment, a function generator (HP33250A, Agilent Technologies, Santa Clara, CA) was used to supply the source signals that were amplified by a 50 dB radio frequency (RF) amplifier (350L, ENI Technology Inc., Rochester, NY) and then delivered to the HIFU transducer in order to induce thermal lesions in the target with or without laser illumination. We used HIFU waves with 95% duty cycle and 5 Hz repetition rate to ablate the target tissue. In the experiments, the cavitation signals detected by the PCD transducer were amplified by a pre-amplifier (5072PR, OlympusNDT, Waltham, MA), and collected by a data acquisition card (GageScope, CS21G8256MSn Gage, Lockport, IL). The PCD received the signals from the scattered sound consisted of primary 5 MHz waves from HIFU and the other signals emitted from cavitation, which consisted of higher harmonics. Therefore, a 10 MHz of high-pass filter was used to remove contributions from the HIFU fundamental and second harmonic frequencies. The temperature was measured by the thermocouple through a measurement system (Omega, OMB-DAQ-2416, Stamford, CT) that collected temperature data in 10 Hz rate.

We conducted experiments in two different treatment depths, which are 2 mm and 9 mm from the skin surface, respectively. In these depths, three HIFU pressures (6.2 MPa, 7.9 MPa, and 9.8 MPa) were employed on the target region. The corresponding HIFU focal pressures at different depths were obtained from a finite difference time domain (FDTD) algorithm using acoustical properties of the tissue sample (1540 m/s and 0.3 Np/cm at 5 MHz). Two wavelengths of laser, 532 nm and 760 nm, were applied to achieve deep penetration depth. The laser fluence was first measured at the skin of the animal, and the different incident fluences of laser (20 mJ/cm^2 , for 532 nm, and 25 mJ/cm^2 for 760 nm) were used. Under each condition, 5 trials were conducted for HIFU implementation with laser exposure, and the same number of data was collected from HIFU without laser exposure. The rate of temperature rise during laser-enhanced HIFU was calculated to be compared between different conditions.

6.3 Results

6.3.1 Temperature enhancement

During the experiment, cavitation activity was detected and temperature changes were recorded under different HIFU pressures. The enhancement in temperature rise was calculated for different combinations of laser wavelengths and ultrasound pressures. Figure 6.2 shows an example of the measured temperatures with standard deviation (STD). Figure 6.2(a) shows the results of the average temperatures from three HIFU sonications with and without laser illumination. HIFU was applied at a pressure of 6.2 MPa in the focal regions that is 9 mm deep, and the sonication duration was 2 seconds.

532 nm wavelength light was used for laser illumination. Figure 6.2(b) shows the difference in temperature rise, which has a maximum of $\sim 14^{\circ}\text{C}$, between HIFU with laser and without laser. After HIFU treatments, the animal was sacrificed, and then the photograph of HIFU lesions was taken. Figure 6.3 shows the photograph of HIFU lesions inside the animal's thigh. The visible results of HIFU treatments showed enhanced sizes of the lesions for the laser-enhanced HIFU. The results demonstrate the enhanced HIFU thermal-ablation visually when laser was used concurrently with HIFU treatments.

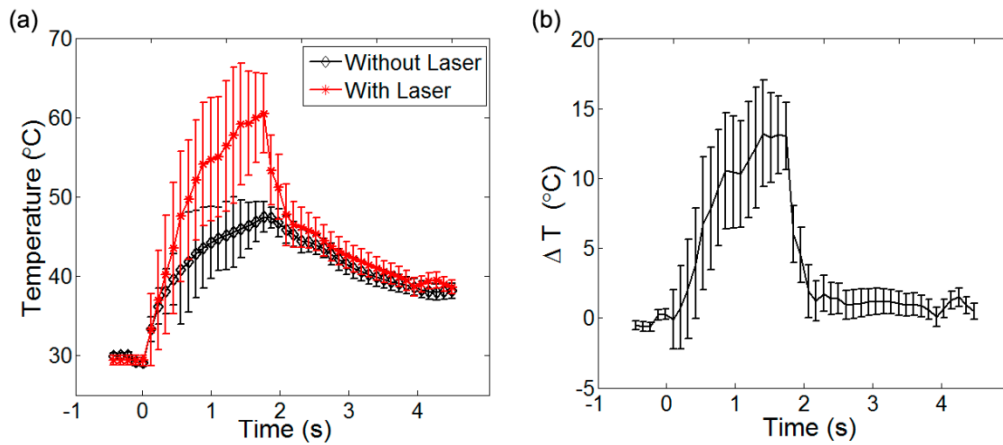


Figure 6.2 Measured Temperatures and error with standard deviation. (a) The time profile of temperature change. (b) The temperature difference between average results from HIFU with and without laser exposure.

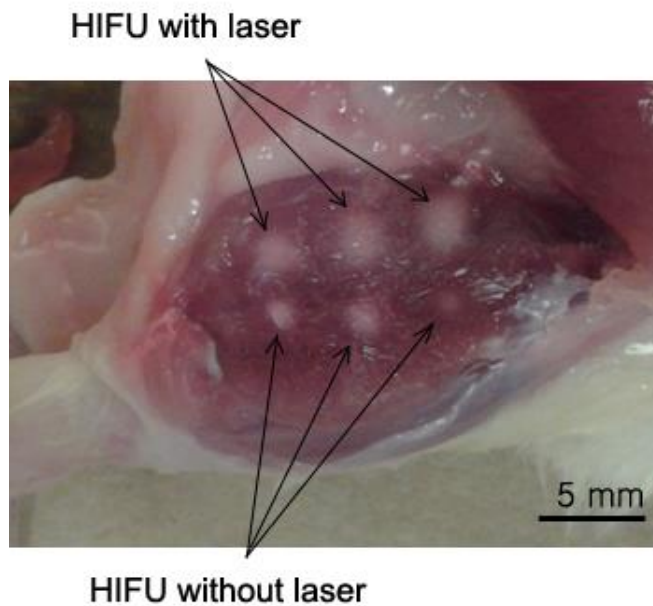


Figure 6.3 Photograph of HIFU lesions. HIFU treatments with laser and without laser were implemented in 5 mm depth from the skin. The leg muscle was cut open to show the enhanced necrosis by HIFU with laser.

Figure 6.4 shows the temperature enhancement rate of laser-enhanced HIFU with different wavelengths, depths and HIFU pressure. The temperature rise from laser-enhanced HIFU was obtained from 5 repeated measurements on several nearby locations for each combination of conditions. To compare temperature enhancements, the temperature enhancement rate was defined as,

$$R = \frac{(\sum_{i=1}^n M_{wl_i})/n - T_0}{(\sum_{i=1}^n M_{wo_i})/n - T_0}, \quad (1)$$

when M_{wl} and M_{wo} are the mean values of changed temperature during HIFU treatment with laser and without laser respectively and T_0 is the base temperature before HIFU treatment. The mean values ($M = \int_0^t T(t)dt / t$) were obtained by from the changed temperature ($T(t)$) for 10 seconds after HIFU starts because the HIFU sonication duration was 10 seconds in these experiments. In two depths (2 mm and 9 mm) and two wavelengths of laser (532 nm and 760 nm), three data sets for different HIFU pressures, which were 6.2 MPa, 7.9 MPa, and 9.8 MPa, were collected and the mean values were presented in Figure 6.4. Most temperature enhancement rates are over 1, which indicates laser exposure during HIFU treatment is effective to enhance temperature rise. In one case (9 mm and 9.8 MPa), however, the average temperature enhancement rate is slightly below 1, indicating there is no temperature enhancement when laser was used. Given the fact that the temperature enhancement at 9.8 MPa was barely above 1 for the rest of three parameter settings, we believe that the results were in the range of errors and indicated that the temperature enhancement rates at high HIFU pressure were insignificant, while the temperature enhancement rates at low HIFU pressure were more significant. This conclusion can be explained by the saturation of cavitation activities/temperature rise at high HIFU pressure. Laser enhances HIFU by inducing more cavitation activities. At low HIFU pressure, the cavitation activity and temperature rise induced by HIFU-only are

very low. When laser is applied and cavitation activity is induced, the temperature rise can be greatly enhanced. However, at high HIFU pressure, the cavitation activity and temperature rise induced by HIFU-only are already very high, and likely reach a saturated level. As a result, the addition of laser light cannot enhance cavitation activity and temperature rise anymore. This explanation is supported by the results shown in Figure 6.4, where the temperature enhanced rates between temperature rises during HIFU with laser light and without laser light were higher at 6.2 MPa and 7.9 MPa than at 9.8 MPa. On the other hand, the differences in results from the two optical wavelengths at different depths were not significant.

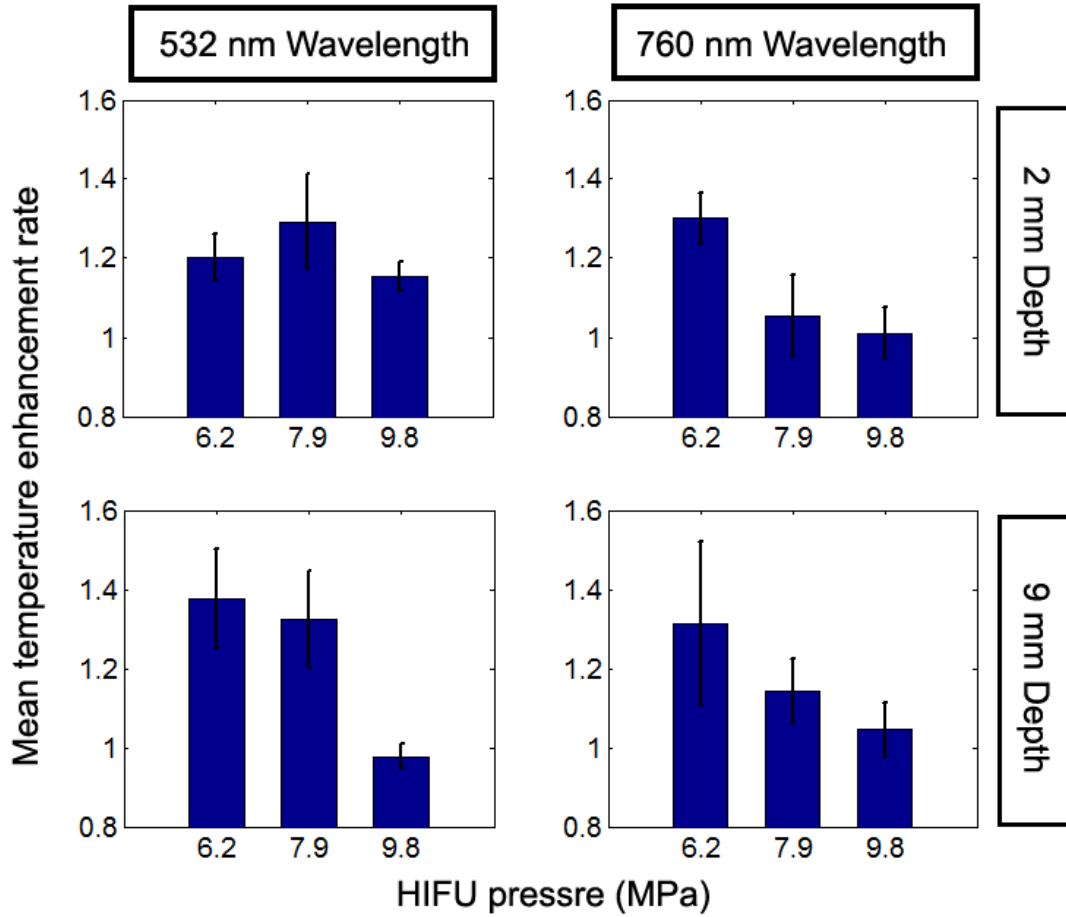


Figure 6.4 Temperature enhancement rates in different wavelengths, depths and HIFU pressure.

Figure 6.5 shows the results for different HIFU durations. Figure 6.5(a) shows the temperature enhancement rate in 2 mm and 9 mm depths for 2 seconds and 10 seconds HIFU duration. The two results for 10 seconds were 1.17 and 1.13, in which the mean value from 2 mm depth was a little higher than 9 mm depth. In the results for 2 seconds,

the mean values were 1.4 and 1.35 for 2 mm and 9 mm depth respectively. The results from different laser wavelengths are shown in Figure 6.5(b). The temperature enhancement rate for 10 seconds using 532 nm wavelength of laser was a little higher than that from 760 nm wavelength.

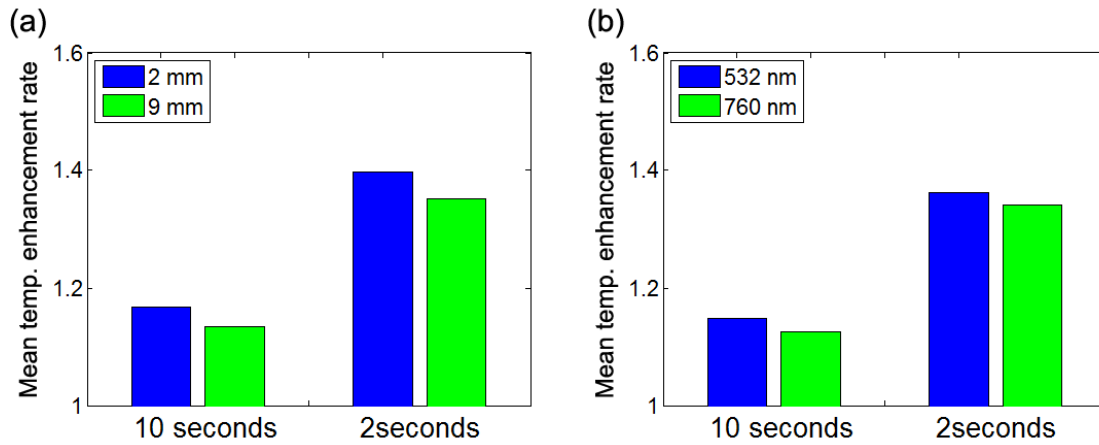


Figure 6.5 Comparison of the temperature enhancement rates for different HIFU durations. (a) The enhancement rates of laser-enhanced HIFU in 2 mm and 9 mm depths for 2 seconds and 10 seconds. (b) The enhancement rates in 532 nm and 760 nm of wavelength of laser for 2 seconds and 10 seconds.

6.32 Cavitation enhancement

We showed that the laser is effective to improve the temperature rise during HIFU treatment. This temperature enhancement is caused by the enhanced cavitation activity. To monitor cavitation activity during HIFU, we used a PCD in the study at each parameter settings. An example of the cavitation signals received by the PCD is shown in Figure 6.6. We observed very weak cavitation signals when the HIFU pressure is relatively low in Figure 6.6(a). However, cavitation acoustic emissions were clearly enhanced while implementing HIFU with laser irradiation at the same time (Figure 6.6(b)). The cavitation signals were detected from the HIFU treatments by using 7.9 MPa HIFU focal pressure at 2 mm depth. For laser exposure, 532 nm wavelength light with 20 mJ/cm² fluence were used. HIFU sonication duration was 2 seconds and cavitation signals were collected for 4 seconds from the start of HIFU treatment. Data collection process was repeated five times both with and without laser exposure. The number of cavitation signals that have acoustic intensity over 100-fold of the initial signal intensity is shown in Table 6.1. Stronger cavitation activities were observed with laser exposure than without laser exposure.

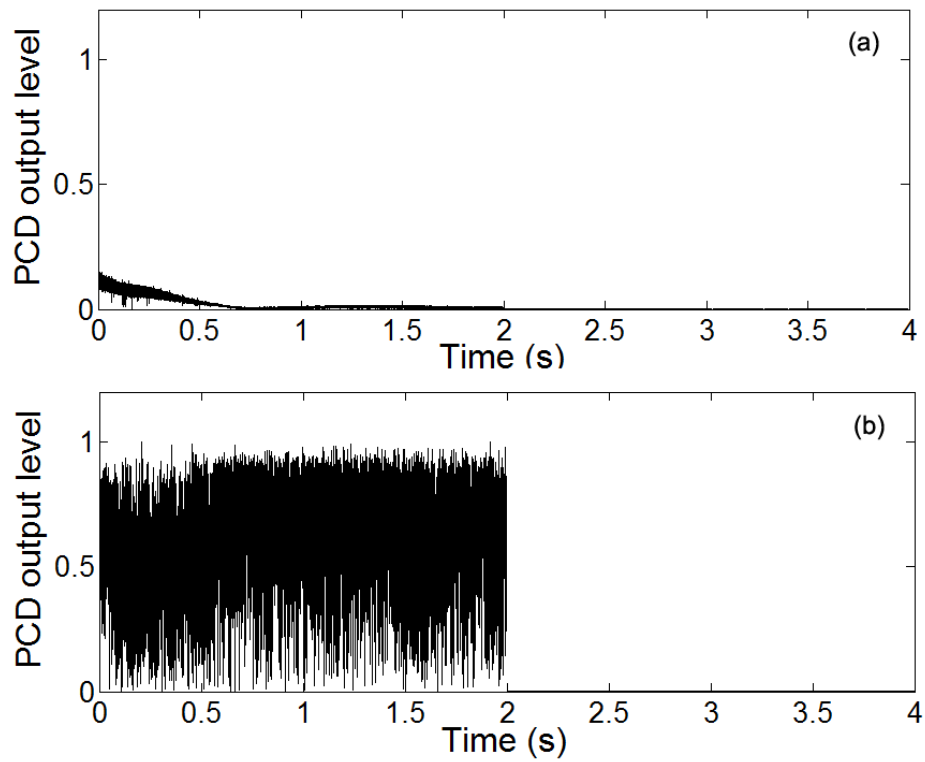


Figure 6.6 Cavitation signals detected by a PCD as a function of time. (a) The signal generated with HIFU -only. (b) The signal generated with HIFU and laser exposure using the same pressure. 20mJ/cm² fluence and 532 nm wavelength laser and 7.9 MPa HIFU pressure were used at 2 mm depth.

Table 6.1 Number of HIFU lesions with clear cavitation acoustic emissions from five HIFU sonications.

Wavelength	2 mm				9 mm			
	760 nm		532 nm		760 nm		532 nm	
	On	Off	On	Off	On	Off	On	Off
6.2 MPa	2	0	2	0	1	0	2	0
7.9 MPa	5	3	5	1	4	2	4	2
9.8 MPa	5	4	5	3	5	4	5	5

At 6.2-MPa HIFU focal pressure, the detected number of cavitation events shows a large difference between laser on and off. Further, the results at 7.9 MPa and 9.8 MPa with laser show relatively low enhancement in cavitation activity as compared with 6.2 MPa. These results can be well correlated with temperature enhancement rates shown in Figure 6.4, where large enhancement was observed at low HIFU pressures and small enhancement was observed at high HIFU pressures between laser on and off.

6.4 Discussion

The result presented in the current study demonstrated that concurrent use of laser illumination can enhance cavitation activity and temperature rise during HIFU therapy. Laser energy has been widely used to nucleate cavitations in clear media with high laser intensity (57, 116). In this study, however, we showed that with the combination of laser and ultrasound, cavitation was enhanced at a relatively low optical fluence, which complies with the laser safety limit for human recommended by American National Standards Institute (45). Therefore, the enhanced cavitation and heating effect showed in this study is likely due to the combination effect of laser and ultrasound, not laser alone.

One possible mechanism is that when laser and HIFU are combined, two pressure components will superpose together. One pressure component is provided by HIFU, and the other by laser through photoacoustic effect. Photoacoustic signals are acoustic waves produced by thermal expansion when laser energy is absorbed by tissue. Generated photoacoustic waves can provide additional pressure to HIFU when they are superposed in phase. As a result, cavitation can be nucleated at a relative low HIFU pressure.

To quantify the additional pressure produced by photoacoustic effect, photoacoustic signals generated from blood were measured. Fresh rat blood was injected in a tygon-tubing with an internal diameter of 1mm and outer diameter of 1.75 mm. Laser light at 532 nm wavelength and 20 mJ/cm² fluence was used. The generated photoacoustic signals were detected by a standard needle hydrophone (DCPS029, Precision Acoustics LTD, Dorchester, UK) in water. Figure 6.7 shows the averaged pressure signal detected at 20-mm distance. The negative peak amplitude was 8.6 kPa

with a center frequency around 10 MHz. By assuming a point photoacoustic source (due to small laser spot) and linear spherical wave propagation, the acoustic pressure at 180 μm distance that is radius of the confocal spot of laser and the transducer was 0.95 MPa. This measurement result indicated that significant additional pressure could be added to HIFU pressure through photoacoustic effect during combined laser and HIFU process.

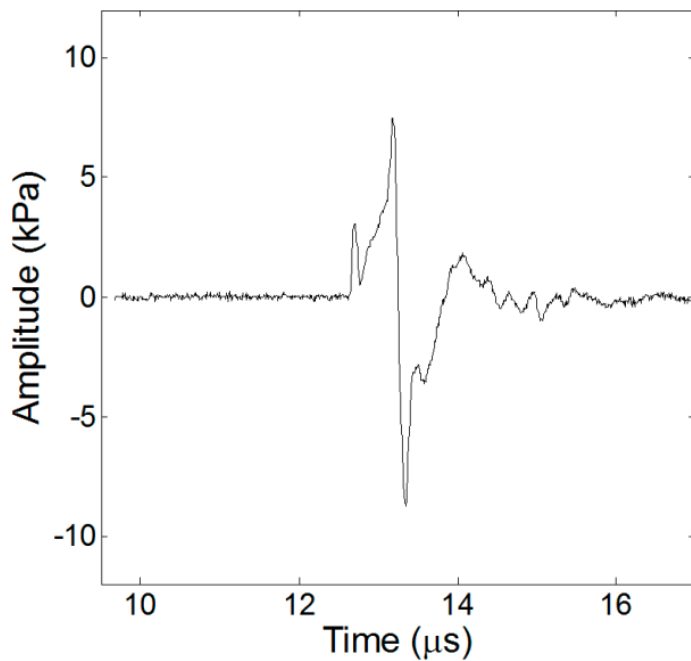


Figure 6.7 Photoacoustic pressure generated from rat blood in a tubing.

To further confirm our measurement, photoacoustic pressure was also estimated through a theoretic approach by using the following equation,

$$p_0 = A_e \Gamma = \mu_a \phi \Gamma, \quad (2)$$

where, Γ denotes Grueneisen parameter, μ_a denotes optical absorption coefficient, and ϕ denotes optical fluence (4). At body temperature (37°C), the Gruneisen parameter Γ is around 0.20 for blood, the absorption coefficient of blood at 532 nm of wavelength is 233 cm^{-1} , when the hemoglobin concentration in blood is typical 150 gHb/liter. If the laser light had a fluence of 20 mJ/cm^2 as we used in the experiments, the calculated photoacoustic pressure was 0.93 MPa by using equation (2). This value agreed very well with the measurement value.

The above results demonstrated that laser light can provide relatively significant addition acoustic pressure (about 1 MPa) to HIFU through photoacoustic effect. The addition acoustic pressure, in combined with the original HIFU pressure, can enhance cavitation activity and the subsequent heating effect.

Using laser to enhance cavitation activity has several advantages. First, it is a particle-free method, and no exogenous contrast bubbles are needed to be injected into blood stream. Second, it can effectively reduce the needed HIFU pressure and enhance heating. Low HIFU pressure and enhanced heating will cause less skin burns and facilitate HIFU treatment process. It is especially important in highly perfused tissues,

where blood cooling effect can significantly limit the outcome of thermal therapy. Additionally, enhanced cavitation effect can improve thrombolysis process and prevent or relieve stroke and thrombosis. Finally, the technique can be easily performed during PAI-guided HIFU therapy where both ultrasound and laser energy are involved.

A limitation with laser-enhanced cavitation during HIFU technique is the treatment depth. Our current and previous results demonstrated a treatment depth of around 1 cm. Deeper treatment depth will require using higher laser fluence, or special method to deliver laser light, such as focusing laser light inside soft tissue, or using fiber optics to deliver laser energy to the target region. The trade-offs these technique needs further investigations.

6.5 Conclusions

In vivo results of laser-enhanced HIFU heating were presented in the current study. The results provided comparisons to show the effects of laser light exposure under various conditions to enhance temperature rise and cavitation activity during HIFU treatment. Laser light is well-known for its ability to nucleate cavitation through vaporization. To vaporize the surrounding fluid through either optical absorption or optical breakdown, high optical intensity is needed. In this study, laser light at the safe power level recommended by ANSI was used during HIFU treatment to enhance the cavitation activity. We demonstrated that laser-enhanced HIFU heating was more effective at relative low HIFU pressure. Therefore, the combination of ultrasound and laser is the main point for cavitation. Concurrent light illumination during HIFU has the

potential to enhance cavitation by reducing cavitation threshold. Furthermore, this study presents an advance method without the use of any nano-particles or contrast agents.

Chapter 7 Conclusions

7.1 Summary and Conclusions

In this work, we have described the capability and potential of PA imaging and laser-enhanced HIFU which are biomedical applications using optics and acoustics. The advantages of PA imaging are the combination of the high contrast of optical imaging and the high resolution of ultrasound imaging and the ability of non-invasive functional imaging. We have achieved interesting results in the study of functional PA imaging via *in vivo* animal experiments. Additionally, we studied how to improve the effectiveness of HIFU treatments applying optics. And the enhanced result was shown by using *in vivo* murine animal models. These results demonstrate the high feasibility of using optics and acoustics in the biomedical area.

7.1.1 The results of PA imaging

To detect brain activity, PA imaging systems were used in the studies. The cerebral cortex of a Sprague-Dawley rat was imaged by a PAT system to detect the pharmacological effects of cocaine hydrochloride. Different concentrations (1, 2.5, and 5.0 mg per kg body weight) of cocaine hydrochloride in saline solution were injected into Sprage-Dawley rats through tail veins. The cerebral cortex images of the rats were continuously obtained by the PAT system. The PA images were compared with each other and confirmed that changes in blood volume were induced by cocaine hydrochloride injection. The study of small animal brain activation in response to drug activity was continued using a PAM system. The rat brain functional change was monitored by PAM technique. Images in the coronal view of the rat brain at the locations

of 1.2 and 3.4 mm posterior to bregma were obtained. The resulting PA images showed the regional changes in the blood volume and blood oxygenation. In addition, the customized PA imaging system was used to detect the neuronal activity in the motor cortex of a rhesus monkey during forelimb movement. PA images were acquired through a 30-mm diameter implanted cranial chamber. Increased PA signal amplitude arises from an increase in regional blood volume and these results indicate increased neuronal activity. These results demonstrate the feasibility of utilizing PA imaging for studies of functional activation of the cerebral cortex in animal models.

7.1.2 The results of laser-enhanced HIFU

The enhanced cavitation activities and heating during HIFU treatment with concurrent use of laser illumination were investigated by using *in vivo* animal models. The thighs of murine animals were concurrently irradiated by HIFU and pulsed-laser with different optical wavelengths and acoustic pressures. The temperature increases in HIFU focal regions were measured by inserting thermocouples and the cavitation signals were detected by a passive cavitation detector. The results showed the efficacy and potential of laser-enhanced HIFU in this study.

7.2 Future Work

As novel studies using optics and acoustics, PA imaging and HIFU technique will be spread widely in biomedical research, clinical applications and theoretical and experimental work. In order to improve and optimize the techniques for clinical utility, we need further studies.

7.2.1 Contrast agent for absorption

Optical imaging can provide both functional and anatomical information with excellent contrast between tissue types using exogenously delivered contrast agents. High optical absorbing contrast agents can be employed to enhance PA imaging, although the PA signal is sensitive to endogenous molecules such as hemoglobin or melanin (117, 118). Contrast agents like nanoparticles with strong optical absorption have already been investigated in medicine today. In the case of laser-enhanced HIFU, the heating effects from optical sources and high intensity ultrasound can be increased with contrast agents for optical and ultrasound absorption. Ultrasound contrast agents have also been considered to constitute an efficient medium for changing acoustic characteristics and improving energy deposition in the focal region (119). We need to enhance the research through the use of contrast agents.

7.2.2 Application for humans

In this work, the techniques of PA imaging and HIFU were studied by means of *in vivo* animal experiments. Most clinical techniques have the purpose of potential utility in human medicine. Although these diagnostic and therapeutic studies used murine and primate animals which are the best animal models for brain research, the goal of this work is also ultimately to develop applications for humans. In order to fulfill this goal, light sources in safety ranges such as NIR light and radio-frequency microwave will be adopted. The design of PA imaging systems and HIFU treatments should be suitable for the human body. Optical imaging – including PA imaging – has been applied to human diagnosis. However, the cranial bone is still a major problem for optical human brain imaging. HIFU has also been used for human treatments for over 40 years although it has

limitations for, among other things, lung disease. These are some of the challenges we have to solve in a future study.

7.2.3 Other techniques using optics and acoustics

We have investigated PA imaging for brain research and the improvement of HIFU treatment using lasers. Both applications demonstrate the use of optics and acoustics for biomedical techniques. The advantages of optics and acoustics are combined and applied to diagnostic and therapeutic studies, and the enhanced results were obtained in this work. However, there are many novel and compelling modalities which are based on optics or acoustics in the biomedical field. I hope to study other techniques and develop the applications to improve the quality, convenience, and utility for patients and researchers.

Bibliography

1. Hebden JC, Arridge SR, Delpy DT. Optical imaging in medicine: I. Experimental techniques. *Physics in medicine and biology*. 1997;42(5):825-40. PubMed PMID: 9172262.
2. Hillman EM, Amoozegar CB, Wang T, McCaslin AF, Bouchard MB, Mansfield J, Levenson RM. In vivo optical imaging and dynamic contrast methods for biomedical research. *Philos Trans A Math Phys Eng Sci*. 2011;369(1955):4620-43. doi: 10.1098/rsta.2011.0264. PubMed PMID: 22006910 PMCID: PMC3263788.
3. Licha K. Contrast Agents for Optical Imaging. In: Krause W, editor. *Contrast Agents II*: Springer Berlin Heidelberg; 2002. p. 1-29.
4. Wang LV, Wu H-i. *Biomedical optics : principles and imaging*. Hoboken, N.J.: Wiley-Interscience; 2007. xiv, 362 p. p.
5. Luker GD, Luker KE. Optical imaging: current applications and future directions. *Journal of nuclear medicine : official publication, Society of Nuclear Medicine*. 2008;49(1):1-4. doi: 10.2967/jnumed.107.045799. PubMed PMID: 18077528.
6. Xu MH, Wang LHV. Photoacoustic imaging in biomedicine. *Review of Scientific Instruments*. 2006;77(4). doi: Artn 041101
Doi 10.1063/1.2195024. PubMed PMID: WOS:000237136500001.
7. Li C, Wang LV. Photoacoustic tomography and sensing in biomedicine. *Physics in medicine and biology*. 2009;54(19):R59-97. Epub 2009/09/03. doi: 10.1088/0031-9155/54/19/R01. PubMed PMID: 19724102 PMCID: PMC2872141.

8. Su YX, Zhang F, Xu KX, Yao JQ, Wang RKK. A photoacoustic tomography system for imaging of biological tissues. *J Phys D Appl Phys.* 2005;38(15):2640-4. doi: Doi 10.1088/0022-3727/38/15/016. PubMed PMID: WOS:000231406800017.
9. Beard P. Biomedical photoacoustic imaging. *Interface focus.* 2011;1(4):602-31. Epub 2012/08/07. doi: 10.1098/rsfs.2011.0028. PubMed PMID: 22866233 PMCID: PMC3262268.
10. Bell AG. On the production and reproduction of sound by light. *American Journal of Science.* 1880;s3-20(118):305-24. doi: 10.2475/ajs.s3-20.118.305.
11. Kruger RA, Liu P, Fang YR, Appledorn CR. Photoacoustic ultrasound (PAUS)--reconstruction tomography. *Medical physics.* 1995;22(10):1605-9. Epub 1995/10/01. PubMed PMID: 8551984.
12. Hoelen CG, de Mul FF, Pongers R, Dekker A. Three-dimensional photoacoustic imaging of blood vessels in tissue. *Optics letters.* 1998;23(8):648-50. PubMed PMID: 18084605.
13. Oraevsky AA, Andreev VA, Karabutov AA, Fleming RD, Gatalica Z, Singh H, Esenaliev RO, editors. *Laser optoacoustic imaging of the breast: detection of cancer angiogenesis* 1999.
14. Ku G, Wang LV. Scanning thermoacoustic tomography in biological tissue. *Medical physics.* 2000;27(5):1195-202. PubMed PMID: 10841427.
15. Duck FA. *Physical Properties of Tissue: A Comprehensive Reference Book:* Institution of Physics & Engineering in Medicine & Biology; 2012.
16. Esenaliev RO, Karabutov AA, Oraevsky AA. Sensitivity of laser opto-acoustic imaging in detection of small deeply embedded tumors. *Ieee J Sel Top Quant.*

1999;5(4):981-8. doi: Doi 10.1109/2944.796320. PubMed PMID:

WOS:000083257800016.

17. Mallidi S, Luke GP, Emelianov S. Photoacoustic imaging in cancer detection, diagnosis, and treatment guidance. *Trends in biotechnology*. 2011;29(5):213-21. doi: 10.1016/j.tibtech.2011.01.006. PubMed PMID: 21324541 PMCID: PMC3080445.
18. Villringer A, Chance B. Non-invasive optical spectroscopy and imaging of human brain function. *Trends in neurosciences*. 1997;20(10):435-42. PubMed PMID: 9347608.
19. Grinvald A, Frostig RD, Lieke E, Hildesheim R. Optical imaging of neuronal activity. *Physiological reviews*. 1988;68(4):1285-366. PubMed PMID: 3054949.
20. Laufer J, Elwell C, Delpy D, Beard P. In vitro measurements of absolute blood oxygen saturation using pulsed near-infrared photoacoustic spectroscopy: accuracy and resolution. *Physics in medicine and biology*. 2005;50(18):4409-28. doi: Doi 10.1088/0031-9155/50/18/011. PubMed PMID: WOS:000232427800011.
21. Sivaramakrishnan M, Maslov K, Zhang HF, Stoica G, Wang LV. Limitations of quantitative photoacoustic measurements of blood oxygenation in small vessels. *Physics in medicine and biology*. 2007;52(5):1349-61. doi: 10.1088/0031-9155/52/5/010. PubMed PMID: 17301459.
22. Frostig RD, Lieke EE, Tso DY, Grinvald A. Cortical Functional Architecture and Local Coupling between Neuronal-Activity and the Microcirculation Revealed by In vivo High-Resolution Optical Imaging of Intrinsic Signals. *Proceedings of the National Academy of Sciences of the United States of America*. 1990;87(16):6082-6. doi: DOI 10.1073/pnas.87.16.6082. PubMed PMID: WOS:A1990DU72700016.

23. Stein EW, Maslov K, Wang LHV. Noninvasive, in vivo imaging of blood-oxygenation dynamics within the mouse brain using photoacoustic microscopy. *Journal of biomedical optics*. 2009;14(2). doi: Artn 020502
Doi 10.1117/1.3095799. PubMed PMID: WOS:000266868500002.
24. Yang XM, Skrabalak SE, Li ZY, Xia YN, Wang LHV. Photoacoustic tomography of a rat cerebral cortex in vivo with Au nanocages as an optical contrast agent. *Nano letters*. 2007;7(12):3798-802. doi: Doi 10.1021/NI072349r. PubMed PMID: WOS:000251581600044.
25. Deng Z, Wang Z, Yang X, Luo Q, Gong H. In vivo imaging of hemodynamics and oxygen metabolism in acute focal cerebral ischemic rats with laser speckle imaging and functional photoacoustic microscopy. *Journal of biomedical optics*. 2012;17(8):081415-1. doi: 10.1117/1.JBO.17.8.081415. PubMed PMID: 23224176.
26. Lynn JG, Zwemer RL, Chick AJ, Miller AE. A new method for the generation and use of focused ultrasound in experimental biology. *Journal of General Physiology*. 1943;26(2):179-93. PubMed PMID: WOS:000202068400006.
27. Kennedy JE. High-intensity focused ultrasound in the treatment of solid tumours. *Nature reviews Cancer*. 2005;5(4):321-7. doi: 10.1038/nrc1591. PubMed PMID: 15776004.
28. Kennedy JE, Wu F, ter Haar GR, Gleeson FV, Phillips RR, Middleton MR, Cranston D. High-intensity focused ultrasound for the treatment of liver tumours. *Ultrasonics*. 2004;42(1-9):931-5. doi: 10.1016/j.ultras.2004.01.089. PubMed PMID: 15047409.

29. Rewcastle JC. High intensity focused ultrasound for prostate cancer: a review of the scientific foundation, technology and clinical outcomes. *Technology in cancer research & treatment*. 2006;5(6):619-25. PubMed PMID: 17121439.
30. Kennedy JE, Ter Haar GR, Cranston D. High intensity focused ultrasound: surgery of the future? *The British journal of radiology*. 2003;76(909):590-9. doi: 10.1259/bjr/17150274. PubMed PMID: 14500272.
31. ter Haar G, Coussios C. High intensity focused ultrasound: Physical principles and devices. *International Journal of Hyperthermia*. 2007;23(2):89-104. doi: 10.1080/02656730601186138. PubMed PMID: WOS:000246204900002.
32. Chartier-Kastler E, Yonneau L, Conort P, Haertig A, Bitker MO, Richard F. [High intensity focused ultrasound (HIFU) in urology]. *Progres en urologie : journal de l'Association francaise d'urologie et de la Societe francaise d'urologie*. 2000;10(6):1108-17. PubMed PMID: 11217545.
33. Illing R, Chapman A. The clinical applications of high intensity focused ultrasound in the prostate. *International journal of hyperthermia : the official journal of European Society for Hyperthermic Oncology, North American Hyperthermia Group*. 2007;23(2):183-91. doi: 10.1080/02656730601173037. PubMed PMID: 17578342.
34. Orsi F, Arnone P, Chen W, Zhang L. High intensity focused ultrasound ablation: a new therapeutic option for solid tumors. *J Cancer Res Ther*. 2010;6(4):414-20. doi: 10.4103/0973-1482.77064. PubMed PMID: 21358073.
35. Wu F, ter Haar G, Chen WR. High-intensity focused ultrasound ablation of breast cancer. *Expert Rev Anticancer Ther*. 2007;7(6):823-31. doi: 10.1586/14737140.7.6.823. PubMed PMID: 17555392.

36. Hill CR, terHaar GR. Review article: High intensity focused ultrasound-potential for cancer treatment. *British Journal of Radiology*. 1995;68(816):1296-303. PubMed PMID: WOS:A1995TL75800002.
37. Andlin-Sobocki P, Rehm J. Cost of addiction in Europe. *European journal of neurology : the official journal of the European Federation of Neurological Societies*. 2005;12 Suppl 1:28-33. doi: 10.1111/j.1468-1331.2005.01194.x. PubMed PMID: 15877775.
38. Grant BF, Dawson DA. Age of onset of drug use and its association with DSM-IV drug abuse and dependence: Results from the National Longitudinal Alcohol Epidemiologic Survey. *Journal of Substance Abuse*. 1998;10(2):163-73. doi: Doi 10.1016/S0899-3289(99)80131-X. PubMed PMID: WOS:000077362200005.
39. Volkow N, Li TK. The neuroscience of addiction. *Nat Neurosci*. 2005;8(11):1429-30. doi: 10.1038/nn1105-1429. PubMed PMID: 16251981.
40. Kruger RA, Reinecke DR, Kruger GA. Thermoacoustic computed tomography-technical considerations. *Medical physics*. 1999;26(9):1832-7. doi: Doi 10.1118/1.598688. PubMed PMID: WOS:000082632200013.
41. Wang LV. Tutorial on photoacoustic microscopy and computed tomography. *Ieee J Sel Top Quant*. 2008;14(1):171-9. doi: Doi 10.1109/Jstqe.2007.913398. PubMed PMID: WOS:000253558100023.
42. Ku G, Wang LV. Deeply penetrating photoacoustic tomography in biological tissues enhanced with an optical contrast agent. *Optics letters*. 2005;30(5):507-9. PubMed PMID: 15789718.

43. Wang X, Xie X, Ku G, Wang LV, Stoica G. Noninvasive imaging of hemoglobin concentration and oxygenation in the rat brain using high-resolution photoacoustic tomography. *Journal of biomedical optics*. 2006;11(2):024015. Epub 2006/05/06. doi: 10.1117/1.2192804. PubMed PMID: 16674205.
44. Wang X, Pang Y, Ku G, Xie X, Stoica G, Wang LV. Noninvasive laser-induced photoacoustic tomography for structural and functional in vivo imaging of the brain. *Nature biotechnology*. 2003;21(7):803-6. Epub 2003/06/17. doi: 10.1038/nbt839. PubMed PMID: 12808463.
45. American National Standard for Safe Use of Lasers ANSI Z136.1-2000, (2000).
46. Ku G, Wang X, Stoica G, Wang LV. Multiple-bandwidth photoacoustic tomography. *Physics in medicine and biology*. 2004;49(7):1329-38. Epub 2004/05/07. PubMed PMID: 15128208.
47. Luo F, Schmidt KF, Fox GB, Ferris CF. Differential responses in CBF and CBV to cocaine as measured by fMRI: implications for pharmacological MRI signals derived oxygen metabolism assessment. *J Psychiatr Res*. 2009;43(12):1018-24. doi: 10.1016/j.jpsychires.2008.11.009. PubMed PMID: 19135215.
48. Yang X, Wang LV. Monkey brain cortex imaging by photoacoustic tomography. *Journal of biomedical optics*. 2008;13(4):044009. Epub 2008/11/22. doi: 10.1117/1.2967907. PubMed PMID: 19021337.
49. Song KH, Wang LV. Deep reflection-mode photoacoustic imaging of biological tissue. *Journal of biomedical optics*. 2007;12(6):060503. doi: 10.1117/1.2818045. PubMed PMID: 18163798.

50. Anthony JC, Petronis KR. Early-onset drug use and risk of later drug problems. *Drug Alcohol Depend.* 1995;40(1):9-15. PubMed PMID: 8746919.
51. Schwartz BG, Rezkalla S, Kloner RA. Cardiovascular effects of cocaine. *Circulation.* 2010;122(24):2558-69. doi: 10.1161/CIRCULATIONAHA.110.940569. PubMed PMID: 21156654.
52. Cregler LL, Mark H. Medical complications of cocaine abuse. *The New England journal of medicine.* 1986;315(23):1495-500. doi: 10.1056/NEJM198612043152327. PubMed PMID: 3537786.
53. Lu H, Xi ZX, Gitajn L, Rea W, Yang Y, Stein EA. Cocaine-induced brain activation detected by dynamic manganese-enhanced magnetic resonance imaging (MEMRI). *Proceedings of the National Academy of Sciences of the United States of America.* 2007;104(7):2489-94. Epub 2007/02/09. doi: 10.1073/pnas.0606983104. PubMed PMID: 17287361 PMCID: PMC1892936.
54. Volkow ND, Mullani N, Gould KL, Adler S, Krajewski K. Cerebral blood flow in chronic cocaine users: a study with positron emission tomography. *The British journal of psychiatry : the journal of mental science.* 1988;152:641-8. PubMed PMID: 3262397.
55. Jo J, Yang X. Detection of cocaine induced rat brain activation by photoacoustic tomography. *Journal of neuroscience methods.* 2011;195(2):232-5. doi: 10.1016/j.jneumeth.2010.12.006. PubMed PMID: 21163301 PMCID: PMC3026864.
56. Kuhar MJ, Ritz MC, Boja JW. The dopamine hypothesis of the reinforcing properties of cocaine. *Trends in neurosciences.* 1991;14(7):299-302. PubMed PMID: 1719677.

57. Lauterbo.W. Laser-Induced Cavitation. *Acustica*. 1974;31(2):51-78. PubMed PMID: WOS:A1974T943800001.
58. Cui H, Staley J, Yang X. Integration of photoacoustic imaging and high-intensity focused ultrasound. *Journal of biomedical optics*. 2010;15(2):021312. doi: 10.1117/1.3365948. PubMed PMID: 20459234.
59. Kim C, Favazza C, Wang LV. In vivo photoacoustic tomography of chemicals: high-resolution functional and molecular optical imaging at new depths. *Chemical reviews*. 2010;110(5):2756-82. doi: 10.1021/cr900266s. PubMed PMID: 20210338 PMCID: PMC2872199.
60. Liao LD, Li ML, Lai HY, Shih YY, Lo YC, Tsang S, Chao PC, Lin CT, Jaw FS, Chen YY. Imaging brain hemodynamic changes during rat forepaw electrical stimulation using functional photoacoustic microscopy. *NeuroImage*. 2010;52(2):562-70. doi: 10.1016/j.neuroimage.2010.03.065. PubMed PMID: 20362680.
61. Du C, Tully M, Volkow ND, Schiffer WK, Yu M, Luo Z, Koretsky AP, Benveniste H. Differential effects of anesthetics on cocaine's pharmacokinetic and pharmacodynamic effects in brain. *The European journal of neuroscience*. 2009;30(8):1565-75. doi: 10.1111/j.1460-9568.2009.06931.x. PubMed PMID: 19821842 PMCID: PMC2775450.
62. Schmidt KF, Febo M, Shen Q, Luo F, Sicard KM, Ferris CF, Stein EA, Duong TQ. Hemodynamic and metabolic changes induced by cocaine in anesthetized rat observed with multimodal functional MRI. *Psychopharmacology*. 2006;185(4):479-86. Epub 2006/03/22. doi: 10.1007/s00213-006-0319-1. PubMed PMID: 16550388 PMCID: PMC2949961.

63. Marota JJ, Mandeville JB, Weisskoff RM, Moskowitz MA, Rosen BR, Kosofsky BE. Cocaine activation discriminates dopaminergic projections by temporal response: an fMRI study in Rat. *NeuroImage*. 2000;11(1):13-23. doi: 10.1006/nimg.1999.0520. PubMed PMID: 10686113.
64. Yuan Z, Luo Z, Volkow ND, Pan Y, Du C. Imaging separation of neuronal from vascular effects of cocaine on rat cortical brain in vivo. *NeuroImage*. 2011;54(2):1130-9. doi: 10.1016/j.neuroimage.2010.08.045. PubMed PMID: 20804849 PMCID: PMC2997146.
65. D'Esposito M, Deouell LY, Gazzaley A. Alterations in the BOLD fMRI signal with ageing and disease: a challenge for neuroimaging. *Nature reviews Neuroscience*. 2003;4(11):863-72. doi: 10.1038/nrn1246. PubMed PMID: 14595398.
66. Orban GA, Van Essen D, Vanduffel W. Comparative mapping of higher visual areas in monkeys and humans. *Trends Cogn Sci*. 2004;8(7):315-24. doi: 10.1016/j.tics.2004.05.009. PubMed PMID: 15242691.
67. Voytko ML. Functional and neurobiological similarities of aging in monkeys and humans. *Age (Omaha)*. 1997;20(1):29-44. doi: 10.1007/s11357-997-0003-3. PubMed PMID: 23604289 PMCID: PMC3456079.
68. Sani S, Traul D, Klink A, Niaraki N, Gonzalo-Ruiz A, Wu CK, Geula C. Distribution, progression and chemical composition of cortical amyloid-beta deposits in aged rhesus monkeys: similarities to the human. *Acta Neuropathol*. 2003;105(2):145-56. doi: 10.1007/s00401-002-0626-5. PubMed PMID: 12536225.

69. Griffin DM, Hudson HM, Belhaj-Saif A, Cheney PD. Stability of output effects from motor cortex to forelimb muscles in primates. *J Neurosci*. 2009;29(6):1915-27. doi: 10.1523/JNEUROSCI.4831-08.2009. PubMed PMID: 19211898 PMCID: PMC2713178.
70. Grinvald A, Frostig RD, Siegel RM, Bartfeld E. High-resolution optical imaging of functional brain architecture in the awake monkey. *Proceedings of the National Academy of Sciences of the United States of America*. 1991;88(24):11559-63. doi: 10.1073/pnas.88.24.11559. PubMed PMID: 1763070 PMCID: PMC53175.
71. Vnek N, Ramsden BM, Hung CP, Goldman-Rakic PS, Roe AW. Optical imaging of functional domains in the cortex of the awake and behaving monkey. *Proceedings of the National Academy of Sciences of the United States of America*. 1999;96(7):4057-60. doi: 10.1073/pnas.96.7.4057. PubMed PMID: 10097162 PMCID: PMC22419.
72. Wang LV, Hu S. Photoacoustic tomography: in vivo imaging from organelles to organs. *Science*. 2012;335(6075):1458-62. doi: 10.1126/science.1216210. PubMed PMID: 22442475 PMCID: PMC3322413.
73. Jo J, Yang X. Functional photoacoustic imaging to observe regional brain activation induced by cocaine hydrochloride. *Journal of biomedical optics*. 2011;16(9):090506. Epub 2011/09/29. doi: 10.1117/1.3626576. PubMed PMID: 21950909 PMCID: PMC3189975.
74. Zhang HF, Maslov K, Stoica G, Wang LV. Functional photoacoustic microscopy for high-resolution and noninvasive in vivo imaging. *Nature biotechnology*. 2006;24(7):848-51. doi: 10.1038/nbt1220. PubMed PMID: 16823374.
75. Nie L, Guo Z, Wang LV. Photoacoustic tomography of monkey brain using virtual point ultrasonic transducers. *Journal of biomedical optics*. 2011;16(7):076005.

Epub 2011/08/03. doi: 10.1117/1.3595842. PubMed PMID: 21806266 PMCID: PMC3144974.

76. Oraevsky AA, Nie L, Huang C, Guo Z, Anastasio M, Wang LV, Wang LV. Transcranial photoacoustic tomography of the monkey brain. *Proc SPIE 8223, Photons Plus Ultrasound: Imaging and Sensing 2012*. 2012;8223:82230L. doi: 10.1117/12.907060.

77. Pan D, Pramanik M, Senpan A, Allen JS, Zhang H, Wickline SA, Wang LV, Lanza GM. Molecular photoacoustic imaging of angiogenesis with integrin-targeted gold nanobeacons. *FASEB journal : official publication of the Federation of American Societies for Experimental Biology*. 2011;25(3):875-82. Epub 2010/11/26. doi: 10.1096/fj.10-171728. PubMed PMID: 21097518 PMCID: PMC3042842.

78. Staley J, Grogan P, Samadi AK, Cui H, Cohen MS, Yang X. Growth of melanoma brain tumors monitored by photoacoustic microscopy. *Journal of biomedical optics*. 2010;15(4):040510. doi: 10.1117/1.3478309. PubMed PMID: 20799777.

79. Jo J, Zhang H, Cheney PD, Yang X. Photoacoustic detection of functional responses in the motor cortex of awake behaving monkey during forelimb movement. *Journal of biomedical optics*. 2012;17(11):110503. doi: 10.1117/1.JBO.17.11.110503. PubMed PMID: 23089667 PMCID: PMC3477655.

80. Erpelding TN, Kim C, Pramanik M, Jankovic L, Maslov K, Guo Z, Margenthaler JA, Pashley MD, Wang LV. Sentinel lymph nodes in the rat: noninvasive photoacoustic and US imaging with a clinical US system. *Radiology*. 2010;256(1):102-10. doi: 10.1148/radiol.10091772. PubMed PMID: 20574088 PMCID: PMC2897692.

81. Laufer J, Cox B, Zhang E, Beard P. Quantitative determination of chromophore concentrations from 2D photoacoustic images using a nonlinear model-based inversion scheme. *Applied optics*. 2010;49(8):1219-33. PubMed PMID: WOS:000275390200006.
82. Saratoon T, Tarvainen T, Cox BT, Arridge SR. A gradient-based method for quantitative photoacoustic tomography using the radiative transfer equation. *Inverse Problems*. 2013;29(7). doi: Artn 075006
Doi 10.1088/0266-5611/29/7/075006. PubMed PMID: WOS:000321183800006.
83. Treeby BE. Acoustic attenuation compensation in photoacoustic tomography using time-variant filtering. *Journal of biomedical optics*. 2013;18(3):036008. doi: 10.1117/1.JBO.18.3.036008. PubMed PMID: 23503580.
84. Dean-Ben XL, Razansky D, Ntziachristos V. The effects of acoustic attenuation in optoacoustic signals. *Physics in medicine and biology*. 2011;56(18):6129-48. doi: 10.1088/0031-9155/56/18/021. PubMed PMID: 21873768.
85. White AR, Palm P, Plonjes E, Subramaniam VV, Adamovich IV. Effect of electron density on shock wave propagation in optically pumped plasmas. *Journal of applied physics*. 2002;91(5):2604-10. doi: Doi 10.1063/1.1435829. PubMed PMID: WOS:000174182400007.
86. Sun JM, Gerstman BS, Li B. Bubble dynamics and shock waves generated by laser absorption of a photoacoustic sphere. *Journal of applied physics*. 2000;88(5):2352-62. doi: Doi 10.1063/1.1288507. PubMed PMID: WOS:000088796500029.
87. Beveridge AC, McGrath TE, Diebold GJ, Karabutov AA. Photoacoustic shock generation in carbon suspensions. *Applied physics letters*. 1999;75(26):4204-6. doi: Doi 10.1063/1.125583. PubMed PMID: WOS:000084504700053.

88. Sheu YL, Li PC. Simulations of photoacoustic wave propagation using a finite-difference time-domain method with Berenger's perfectly matched layers. *The Journal of the Acoustical Society of America*. 2008;124(6):3471-80. doi: 10.1121/1.3003087. PubMed PMID: 19206776.
89. Wang LV. Tutorial on Photoacoustic Microscopy and Computed Tomography. *Selected Topics in Quantum Electronics, IEEE Journal of*. 2008;14(1):171-9. doi: 10.1109/JSTQE.2007.913398.
90. Blackstock DT. Propagation of Plane Sound Waves of Finite Amplitude in Nondissipative Fluids. *Journal of the Acoustical Society of America*. 1962;34(1):9-&. doi: Doi 10.1121/1.1909033. PubMed PMID: WOS:A19622942B00004.
91. Hamilton MF, Blackstock DT. *Nonlinear acoustics*. San Diego, CA: Academic Press; 1998. xviii, 455 p. p.
92. Muhlestein MB, Gee KL, Macedone JH. Educational demonstration of a spherically propagating acoustic shock. *The Journal of the Acoustical Society of America*. 2012;131(3):2422-30. doi: 10.1121/1.3676730. PubMed PMID: 22423789.
93. Blackstock DT. Connection between the Fay and Fubini Solutions for Plane Sound Waves of Finite Amplitude. *The Journal of the Acoustical Society of America*. 1966;39(6):1019. doi: 10.1121/1.1909986. PubMed PMID: ISI:A19667917900001.
94. Khokhlov RV, Soluyan SI, Naugolnych KA. Waves of Moderate Amplitudes in Absorbing Media. *Acustica*. 1964;14(5):248-&. PubMed PMID: WOS:A19642410A00006.
95. Blackstock DT. On Plane Spherical + Cylindrical Sound Waves of Finite Amplitude in Lossless Fluids. *Journal of the Acoustical Society of America*.

1964;36(1):217-&. doi: Doi 10.1121/1.1918941. PubMed PMID:

WOS:A19642964B00006.

96. Carovac A, Smajlovic F, Junuzovic D. Application of ultrasound in medicine. *Acta informatica medica : AIM : journal of the Society for Medical Informatics of Bosnia & Herzegovina : casopis Drustva za medicinsku informatiku BiH*. 2011;19(3):168-71. doi: 10.5455/aim.2011.19.168-171. PubMed PMID: 23408755 PMCID: PMC3564184.
97. Stewart EA, Gostout B, Rabinovici J, Kim HS, Regan L, Tempny CM. Sustained relief of leiomyoma symptoms by using focused ultrasound surgery. *Obstetrics and gynecology*. 2007;110(2 Pt 1):279-87. doi: 10.1097/01.AOG.0000275283.39475.f6. PubMed PMID: 17666601.
98. Dubinsky TJ, Cuevas C, Dighe MK, Kolokythas O, Hwang JH. High-intensity focused ultrasound: current potential and oncologic applications. *AJR American journal of roentgenology*. 2008;190(1):191-9. doi: 10.2214/AJR.07.2671. PubMed PMID: 18094311.
99. Illing RO, Kennedy JE, Wu F, ter Haar GR, Protheroe AS, Friend PJ, Gleeson FV, Cranston DW, Phillips RR, Middleton MR. The safety and feasibility of extracorporeal high-intensity focused ultrasound (HIFU) for the treatment of liver and kidney tumours in a Western population. *British journal of cancer*. 2005;93(8):890-5. doi: 10.1038/sj.bjc.6602803. PubMed PMID: 16189519 PMCID: PMC2361666.
100. Natale A, Pisano E, Shewchik J, Bash D, Fanelli R, Potenza D, Santarelli P, Schweikert R, White R, Saliba W, Kanagaratnam L, Tchou P, Lesh M. First human experience with pulmonary vein isolation using a through-the-balloon circumferential

- ultrasound ablation system for recurrent atrial fibrillation. *Circulation*. 2000;102(16):1879-82. PubMed PMID: 11034932.
101. Lee JD, Huang CH, Yang ST, Chu YH, Shieh YY, Chen JW, Lin KJ. MRI/SPECT-based diagnosis and CT-guided high-intensity focused-ultrasound treatment system in MPTP mouse model of Parkinson's disease. *Medical engineering & physics*. 2013;35(2):222-30. doi: 10.1016/j.medengphy.2012.01.006. PubMed PMID: 22377520.
102. Terhaar GR, Clarke RL, Vaughan MG, Hill CR. Trackless Surgery Using Focused Ultrasound - Technique and Case-Report. *Minim Invasiv Ther*. 1991;1(1):13-9. PubMed PMID: WOS:A1991JH33600002.
103. Yang X, Roy RA, Holt RG. Bubble dynamics and size distributions during focused ultrasound insonation. *The Journal of the Acoustical Society of America*. 2004;116(6):3423-31. PubMed PMID: 15658693.
104. Holt RG, Roy RA. Measurements of bubble-enhanced heating from focused, MHz-frequency ultrasound in a tissue-mimicking material. *Ultrasound in medicine & biology*. 2001;27(10):1399-412. PubMed PMID: 11731053.
105. Coussios CC, Farny CH, Haar GT, Roy RA. Role of acoustic cavitation in the delivery and monitoring of cancer treatment by high-intensity focused ultrasound (HIFU). *International journal of hyperthermia : the official journal of European Society for Hyperthermic Oncology, North American Hyperthermia Group*. 2007;23(2):105-20. PubMed PMID: 17578336.
106. Yang XM, Church CC. Nonlinear dynamics of gas bubbles in viscoelastic media. *Acoust Res Lett Onl*. 2005;6(3):151-6. doi: Doi 10.1121/1.1897824. PubMed PMID: WOS:000230113200009.

107. Hilgenfeldt S, Lohse D, Zomack M. Sound scattering and localized heat deposition of pulse-driven microbubbles. *The Journal of the Acoustical Society of America*. 2000;107(6):3530-9. PubMed PMID: 10875397.
108. Farny CH, Glynn Holt R, Roy RA. The correlation between bubble-enhanced HIFU heating and cavitation power. *IEEE transactions on bio-medical engineering*. 2010;57(1):175-84. doi: 10.1109/TBME.2009.2028133. PubMed PMID: 19651548.
109. Cui H, Zhang T, Yang X. Laser-enhanced cavitation during high intensity focused ultrasound: An study. *Applied physics letters*. 2013;102(13):133702. doi: 10.1063/1.4800780. PubMed PMID: 23653486 PMCID: PMC3631212.
110. Cleveland RO, Sapozhnikov OA, Bailey MR, Crum LA. A dual passive cavitation detector for localized detection of lithotripsy-induced cavitation in vitro. *The Journal of the Acoustical Society of America*. 2000;107(3):1745-58. PubMed PMID: 10738826.
111. Roy RA, Madanshetty SI, Apfel RE. An acoustic backscattering technique for the detection of transient cavitation produced by microsecond pulses of ultrasound. *The Journal of the Acoustical Society of America*. 1990;87(6):2451-8. PubMed PMID: 2373791.
112. Cui HZ, Yang XM. Enhanced-heating effect during photoacoustic imaging-guided high-intensity focused ultrasound. *Applied physics letters*. 2011;99(23). doi: Artn 231113
Doi 10.1063/1.3669441. PubMed PMID: WOS:000298006100013.
113. Cui H, Yang X. Laser enhanced high-intensity focused ultrasound thrombolysis: an in vitro study. *The Journal of the Acoustical Society of America*. 2013;133(2):EL123-8. doi: 10.1121/1.4778375. PubMed PMID: 23363192 PMCID: PMC3562328.

114. Cui H, Yang X. Real-time monitoring of high-intensity focused ultrasound ablations with photoacoustic technique: An in vitro study. *Medical physics*. 2011;38(10):5345-50. doi: 10.1118/1.3638126. PubMed PMID: WOS:000295617400011.
115. Cui HZ, Yang XM. In vivo imaging and treatment of solid tumor using integrated photoacoustic imaging and high intensity focused ultrasound system. *Medical physics*. 2010;37(9):4777-81. doi: Doi 10.1118/1.3480963. PubMed PMID: WOS:000281906000029.
116. Vogel A, Noack J, Nahen K, Theisen D, Busch S, Parlitz U, Hammer DX, Noojin GD, Rockwell BA, Birngruber R. Energy balance of optical breakdown in water at nanosecond to femtosecond time scales. *Applied Physics B-Lasers and Optics*. 1999;68(2):271-80. doi: DOI 10.1007/s003400050617. PubMed PMID: WOS:000078349900018.
117. Grinvald A, Lieke E, Frostig RD, Gilbert CD, Wiesel TN. Functional architecture of cortex revealed by optical imaging of intrinsic signals. *Nature*. 1986;324(6095):361-4. doi: 10.1038/324361a0. PubMed PMID: 3785405.
118. Li W, Brown PK, Wang LV, Xia Y. Gold nanocages as contrast agents for photoacoustic imaging. *Contrast media & molecular imaging*. 2011;6(5):370-7. doi: 10.1002/cmml.439. PubMed PMID: 22025337.
119. Luo W, Zhou X, Tian X, Ren X, Zheng M, Gu K, He G. Enhancement of ultrasound contrast agent in high-intensity focused ultrasound ablation. *Adv Ther*. 2006;23(6):861-8. doi: Doi 10.1007/Bf02850207. PubMed PMID: 17276954.

Vita

Janggun Jo was born in Gwangmyeong, Gyeonggi-do, Korea in 1979. He moved to Jeju island in 1989. He graduated at high school in Jeju city. He started to study in Korea Tech which original name is Korean University of Technology and Education for Bachelor's degree. After undergraduate school in Electronics engineering, he continued his graduate study under instruction of Professor Hyunchan Cho. He received Master's degree in Electronics engineering in 2007. Janggun Jo has experienced working as an instructor in Korean vocational training institutes twice in 2005 and 2007. In 2008, he came to University of Kansas and started to study Bioimaging in 2009. Under the supervision of Dr. Xinmai Yang, he studied optics and acoustics for biomedical application. During Ph.D. Program, he got married with a beautiful woman, SukJung. In 2014, he earned his Ph.D. degree with pleasure.

Permanent address: 889-6 Munhwadong, Gunsansi, Jeonbuk, Korea 573-874